

Integrated assessment of offshore wind power potential using Weather Research and Forecast (WRF) downscaling with Sentinel-1 satellite imagery, optimal sites, annual energy production and equivalent CO₂ reduction



Soklin Tuy ^{a,c}, Han Soo Lee ^{b,*}, Karodine Chreng ^{a,d}

^a Department of Development Technology, Graduate School for International Development and Cooperation (IDEC), Hiroshima University, 1-5-1 Kagamiyama Higashi-Hiroshima, Hiroshima, 739-8529, Japan

^b Transdisciplinary Science and Engineering Program, Graduate School of Advanced Science and Engineering, Hiroshima University, 1-5-1 Kagamiyama, Higashi-Hiroshima, Hiroshima, 738-8529, Japan

^c Business and Distribution Department, Electricité Du Cambodge (EDC), Preah Ang Yukanthor Street, Phnom Penh, Cambodia

^d Corporate Planning and Project Department, Electricité Du Cambodge (EDC), Preah Ang Yukanthor Street, Phnom Penh, Cambodia

ARTICLE INFO

Keywords:

Renewable energy
Cambodia
Exclusive economic zone
Wind power density
Multi-criteria evaluation
Analytic hierarchy process (AHP)
Offshore wind turbine
GE Haliade-X (HX12)
Ocean energy

ABSTRACT

This study aims to assess the offshore wind power potential in Cambodia using the WRF and Sentinel-1 level 2 ocean (L2 OCN) products, to evaluate potential sites and to estimate the annual energy production (AEP) and equivalent CO₂ reduction. The model is initially calibrated and validated against observed onshore winds at four weather stations before its main simulation for the two-years study period of 2018–2019. As a result, the spatially averaged annual wind speed errors between the WRF and L2 OCN data are 0.70 m/s for mean bias error and 0.79 m/s for root mean square error, indicating good model performance. The annual mean wind speeds over the Cambodian Sea are 5.15 m/s, 5.20 m/s and 5.27 m/s at 80 m, 100 m and 140 m above sea level, respectively. Then, analytic hierarchy process (AHP) is applied to evaluate the optimal sites for offshore wind power generation. The most potential areas in Cambodian sea are along Kampot and Kep shoreline. The resulting AEPs are 11,949.02 GWh for 80-m V112 turbines, 20,013.34 GWh for 100-m V164 turbines and 31,880.48 GWh for 150-m HX12 turbines, which could reduce CO₂ emissions by 5.48 Mt-CO₂, 9.18 Mt-CO₂ and 14.63 Mt-CO₂ per year, respectively. If 10% of the total AEP could be generated by 2030, the offshore wind source would contribute to 1.95%, 3.27%, or 5.20% of the country's electric demands forecasted for 2030. The integrated assessment methodology and resources adopted in this study can be applicable to other regions particularly where offshore measurements are not readily available.

1. Introduction

Renewable energy sources (RESs) are the best alternatives to conventional fossil fuels, boosting the economic growth in individual countries. The worldwide shares of RESs continues to increase every year. In 2019, the capacity of renewable power installed globally rose by a new record of 200 GW, most of which originated from solar photovoltaics, making the total installed capacity 2588 GW [1]. In addition to solar photovoltaics, wind is another vastly available RES that has been widely untapped, especially offshore. According to the Global Wind Report 2021 [2], nearly 5% of the wind power installed globally in 2020,

corresponding to more than 35 GW, was from the offshore farms. The importance and potential of offshore wind was emphasized by Ref. [3], who suggested that siting wind turbines in the offshore areas of greatest potential could lead to a surplus in the present global electricity demand. Thus, this RES could be an optimistic answer for power deficit issues and CO₂ emission mitigation. In this regard, many countries have embarked on studying offshore wind resources to determine their advantages.

Offshore wind resources have been assessed in various parts of the globe, such as China [4,5], India [6–8], United States [9], Brazil [10,11], Chile [12,13], and Europe [14,15] by using satellite data and Weather Research and Forecast (WRF) modelling. In mainland Southeast Asia, where most of the sea depths are suitable for offshore projects, the

* Corresponding author.

E-mail addresses: soklin90@gmail.com (S. Tuy), leehs@hiroshima-u.ac.jp (H.S. Lee), karodinec@gmail.com (K. Chreng).

Abbreviations	
AEP	Annual Energy Production
AGL	Above Ground Level
AHP	Analytic Hierarchy Process
ARW	Advanced Research WRF
ASL	Above Sea Level
AWS	Automatic Weather Station
CO ₂	Carbon Dioxide
EAC	Electricity Authority of Cambodia
EEZ	Exclusive Economic Zone
ENW	Equivalent Neutral Wind
GMF	Geophysical Model Function
GN	Gridded Nudging
GoT	Gulf of Thailand
KK	Koh Kong Station
KP	Kampot Station
KPS	Kampong Speu Station
L2 OCN	Level 2 Ocean
MBE	Mean Bias Error
MC2	Mesoscale Compressible Community
NN	No Nudging
NWP	Numerical Weather Prediction
OWI	Ocean Wind Fields
PBL	Planetary Boundary Layer
Q	Water Vapor Mixing Ratio
r	Pearson Correlation Coefficient
RES	Renewable Energy Sources
RMSE	Root Mean Square Error
SAR	Synthetic Aperture Radar
SN	Spectral Nudging
SRTM	Shuttle Radar Topography Mission
STDE	Standard Deviation Error
T	Potential Temperature
TK	Takeo Station
V	Wind Components
WPD	Wind Power Density
WRF	Weather Research and Forecasting

offshore wind potential has been quantified using various methods. In Vietnam, Quang et al. [16] made use of the cross-calibrated multiplatform dataset, whereas Doan et al. [17] simulated the mesoscale WRF model in combination with 25 km-gridded QuickSCAT data, and both yielded similar results that suggested Phy Quy could generate the highest wind energy. Furthermore, Quang et al. [16] suggested that the sea in southern Vietnam should be used for later development due to investment costs and further distances of the potential areas from coastlines. In the Gulf of Thailand (GoT), the WRF model coupled with microscale WAsP and WindSim models [18] and MC2 coupled with a microscale model, MS-Micro [19], were applied to evaluate wind power resources. The models showed agreement that the GoT, particularly in the Bay of Bangkok, has potential for offshore power projects. The coupling method between MC2 and MS-Micro also appeared in Ref. [20], which aimed to assess the offshore wind power in Thailand's western sea. Briefly, the above studies involve the application of numerical weather prediction (NWP), satellite imagery, and global datasets. Their findings indicate that the GoT and nearby sea have potential for offshore energy uptake. For the Cambodian EEZ in the GoT, Tuy et al. [21] performed offshore wind resource mapping using WRF with good agreements with remotely-sensed offshore winds.

NWP models exist under many names, such as RAMS, HIRLAM, ALADIN, and WRF. In terms of research, WRF has been shown to be a good instrument for wind resource evaluation [22,23]. The WRF model offers a wide range of configuration choices. By calibrating the model for appropriate physics and numerical options in the studied areas, the simulated results could be greatly improved [24]. In this sense, many works have investigated the choices of forcing input datasets and numerical, physics, and nudging choices [12,24–31,79]. The previous findings highlighted the sensitivity of WRF for wind simulations: PBL schemes combined with surface layer schemes have a great impact on the model; shorter initialization and higher-resolution domains can improve the output accuracy; driving lateral and boundary condition data types slightly affect the model performance; and the 1-way or 2-way nesting option caused no changes in the results [24,26,29,30,32]. Since PBL schemes are site-specific, their selection requires examination. In terms of nudging techniques, several recommendations are made as follows: long simulations should be run with enabled nudging options above PBL levels; gridded nudging without interior nudging could improve consistency and accuracy; and spectral nudging works well on precipitation downscaling, whereas analysis nudging outperforms 10 m wind speed, 2 m relative humidity, and air humidity [26,27,33,34]. However, Mai et al. [25] noted that due to the suitable nudging option

varying in relation to the studied areas and layers, more research should be conducted. Moreover, it is remains difficult to find a study that evaluates the effect of all nudged variable combinations. Therefore, in this work, the impact of each nudged variable combination and nudging option will be investigated.

Regarding remote-sensing wind fields, satellite-borne sensors consisting of altimeters, scatterometers, and SAR measure backscatters of the sea-surface state are used to invert wind vectors into images with different cell sizes by a geophysical model function (GMF). Although modes vary, the horizontal resolution of SAR data is high, from original cell sizes of a few metres to approximately 75 m for narrow swaths and 400–500 km for widely scanned swaths [35]. Additionally, nearshore wind measurement of the SAR is up to a few hundred metres off the coast despite its accuracy related to distance [36]. Satellites equipped with SAR include Radarsat-1, Radarsat-2, Envisat ASAR, Cosmo Skymed, TerraSar-X, ERS-1, ERS-2, JERS-1, ALOS/PALSAR, Saocom, and Sentinel [37]. The Sentinel-1 mission, whose Sentinel-1A and 1B satellites are operating in orbit, provides three-level data (L0, L1, and L2), and the last two datasets contain offshore wind information. Even though the L2 product provides the readily processed wind vector of the L1 product, only a few studies have used this product. De Montera et al. [38] and Hadjipetrou et al. [39] demonstrated wind vector comparisons between this L2 product and buoys at stations in Ireland and Cyprus, respectively. A similar comparison was implemented in Ref. [40], which concerns the match-up between moored buoys and remote sensing, including data from L2 OCN. None of the research has compared the L2 wind fields to NWP outputs; hence, an attempt is made to do so in this study.

Cambodia, a country in mainland Southeast Asia with a marine border along the GoT, gained a new status as a lower-middle income country in 2015 owing to an annual mean economic growth rate of 8%, which is driven by key sectors, such as the garment industry, agriculture, and tourism [41]. This growth is one of the indicators of energy demand growth. According to the Electricity Authority of Cambodia (EAC) [42], nationwide energy demand increased almost fivefold over that in 2010, reaching 12,499 GWh. EAC also reported that within a total installed capacity of 3896.77 MW, imported power from neighbouring countries accounted for approximately 25%, while hydro- and fossil-fuel power accounted for 45.60% and 45.23% of the total domestic sources, respectively. As hydropower is seasonal, the country's high reliance on it has led to a supply deficit. Thus, to improve system reliability, source diversification should be considered.

The Cambodian potential for RES was shown in Refs. [43–45]. Furthermore, in the wind resource atlas of Southeast Asia, it was

highlighted that the Krovanh Mountain range in southwestern Cambodia and the highly elevated areas near the Vietnamese border in the southeastern province of Kracheh exhibited high wind velocities [46]. Janjai et al. [47] used the KAMM model to create an onshore wind potential map of Cambodia at 50-m height AGL and confirmed similar findings as those in the wind resource atlas. Promsen et al. [48] conducted a microscale wind potential estimation at 50-m and 80-m heights AGL in the Kampot Province with the aid of the WAsP model and concluded that the 15 km × 15 km area centred at a studied meteorological mast was a potential high wind energy location. To the authors' knowledge, estimation of wind potential has never been conducted offshore of Cambodia.

Therefore, the intent of this study is to assess and map the offshore wind potential in Cambodia using the WRF model and remotely sensed data from the Sentinel-1 satellite, to evaluate optimal sites and to quantify the offshore wind energy over the exclusive economic zone (EEZ) of Cambodia for sustainable energy supply and development. The results of the study provide evidence that may draw public attention to this energy source off the coastline and lay a foundation for more comprehensive future research on this resource. The present work is bound within technical feasibility, and therefore, the socio-environmental, economic, and implementation feasibilities are beyond the scope of this study.

2. Study area and materials

2.1. Study area

Cambodia, bordering Thailand to the northwest and Vietnam to the east, has a marine border along the GoT. Four provinces have been established along the coast, namely, Koh Kong, Sihanouk, Kampot, and Kep. The total coastline extends 435 km in length, and the country's EEZ covers a surface area of 42,000 km² [49]. Fig. 1 shows the map of Cambodia with the four meteorological stations and the EEZ of the country considered for offshore wind power estimation in this study.

2.2. Materials

2.2.1. Meteorological data

Ocean wind measurements can be obtained from deployed buoys, ships, coastal weather stations or instruments, such as light detection and ranging and rawinsonde. However, none of these data are available in the Cambodian Sea. Consequently, four AWSs situated further inland are chosen. KP in the Kampot Province and KK in the Koh Kong Province are located approximately 5.3 km and 1.15 km from the coastline, respectively, whereas KPS in the Kampong Speu Province and TK in the Takeo Province are more than 50 km distant from the sea (Fig. 1). The details of each AWS are described in Table 1.

The wind data of the four AWSs were provided by the Department of Meteorology, Ministry of Water Resource and Meteorology for a two-year period from January 01, 2018 to December 31, 2019. The measurements were recorded hourly at 10-m height AGL. As the data are raw data whose quality has not been verified, the data are prone to outliers. To filter these outliers, the boxplot method was employed to avoid distortion of the original time-series pattern.

Table 1

Information on the four AWS sites and elevation differences between the default GTOPO30 topographical data for WRF and the 30-m-gridded SRTM elevation dataset.

AWS	Coordinates (Lat (°N), Lon (°E))	Elevation (m) above sea level	Province	Distance from the shore (km)	Elevation difference (m) (GTOPO30 – SRTM)
Kampot	10.60277, 104.18638	5	coastal	5.3	3.16
Koh Kong	11.60833, 102.98805	5	coastal	1.15	15.03
Kampong Speu	11.47666, 104.58138	32	inland	110.0	-0.29
Takeo	10.97666, 104.79027	9	inland	72.0	1.41

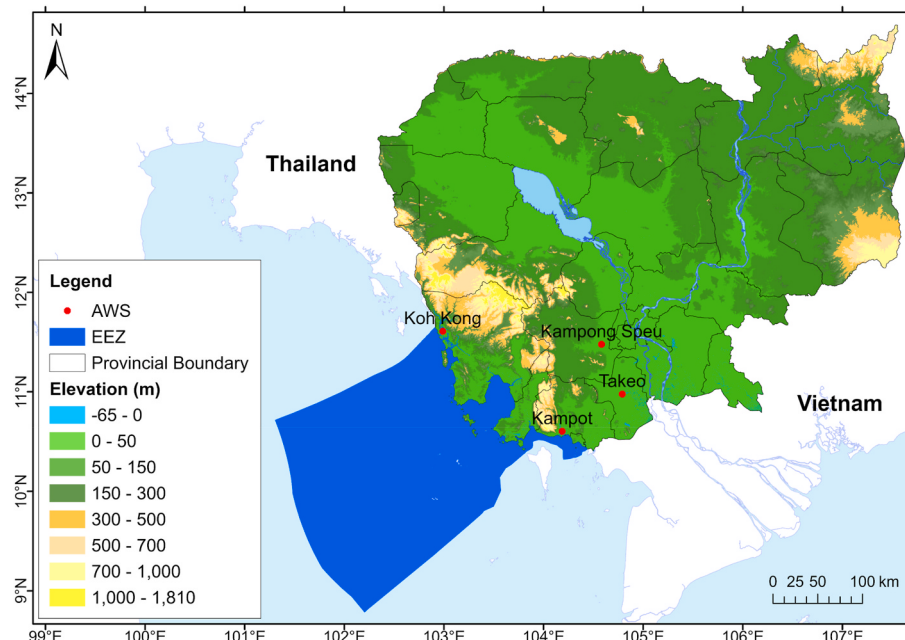


Fig. 1. Map of Cambodia along with the marine exclusive economic zone (EEZ) (blue shade) and onshore and inland automatic weather stations in the Kampot, Koh Kong, Kampong Speu, and Takeo Provinces (red points). (For interpretation of the references to colour in this figure legend, the reader is referred to the Web version of this article.)

2.2.2. Remote-sensing satellite data

The Sentinel-1 mission is the first Earth observatory operation of the European Space Agency for the Copernicus initiative. This mission comprises two satellites: 1A, launched in 2014, and 1B, launched in 2016. Utilized in C-band microwaves, which are insensitive to light level and weather conditions, Sentinel-1A and 1B scan the Earth in four different modes with a high resolution of approximately 5 m and cover a 400-km-wide swath [50]. The two satellites have the same sun-synchronous and near-polar orbits but depart 180° from each other. The satellites have 12-day revisit cycles. The ascending passes of 1A and 1B over the Cambodian EEZ occur at approximately 11:19 to 11:28 UTC, respectively, whereas descending passes occur at approximately 22:53 to 23:02 UTC, respectively.

The images of both satellites have been archived on the Copernicus Open Access Hub website [51] and can be freely accessed. In this study, the L2 OCN product is chosen. The product consists of three elements: the Ocean Wind Fields (OWI), the Radial Surface Velocity, and the Ocean Swell Spectra [52]. The OWI contains ocean wind speed and direction scenes processed from normalized radar cross section of the L1 ground-range-detected product using CMOD-IFR2 GMF; additionally, the grid resolution of the OWI imagery is approximately 1 km [52]. The OWI wind data are the equivalent neutral wind (ENW) measured at 10 m ASL.

Retrieved from the interferometric wide swath mode and dual VV + VH polarization, all the L2 OCN wind scenes are checked to remove error pixels and outliers that could originate from strong ground reflections, such as moving ships. Moreover, the inherent quality flags of the product are 0 for high-quality, 1 for medium-quality, 2 for low-quality, and 3 for poor-quality cells [53]. The valid scenes used in this research are those having pixels flagged with number 3 filtered out. The total number of valid L2 OCN images from January 01, 2018 to December 31, 2019 is 515 samples. The spatial frequency of the samples is depicted in Fig. 2.

3. Method

The procedure of the research was split into two stages: model calibration and core simulation (Fig. 3). The first stage involves sensitivity tests for calibrating physics parameterizations and model setups, whereas the later stage focuses on a long-term two-year simulation to estimate wind resource and offshore wind power potential.

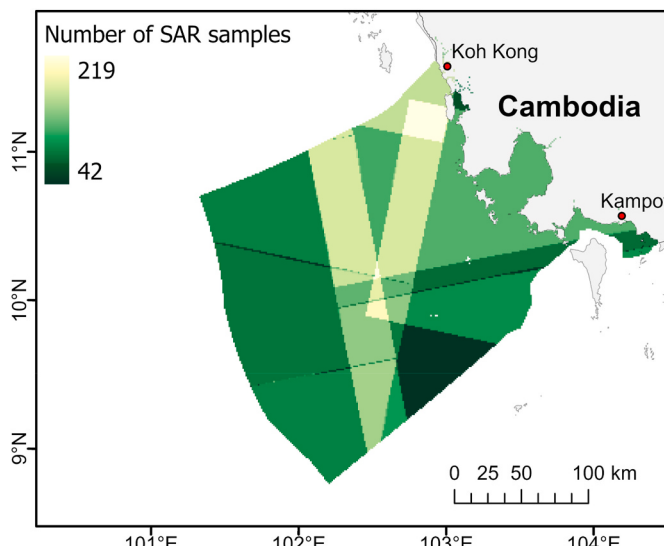


Fig. 2. The number of SAR images distributed over the Cambodian EEZ, sensed by both the Sentinel 1A and 1B satellites for two years from 2018 to 2019.

3.1. WRF setups

The WRF model is one of the mesoscale NWPs capable of atmospheric simulation for research and operational forecasting purposes; moreover, the model operates on two distinctive dynamic cores: ARW, designed by the National Center for Atmospheric Research and Non-hydrostatic Mesoscale Model, created by the National Centers for Environmental Prediction [54]. The former, which based on fully compressible and nonhydrostatic Euler equations, is used in this study. Three domains are created with horizontal grid sizes of 15 km (D01:180 × 190), 5 km (D02:277 × 289), and 1.66 km (D03:298 × 298) (Fig. S1). The area of interest, the EEZ of Cambodia, is completely covered by the innermost domain, D03. For the initial run, the model physical configuration from Ref. [17] is adopted with a modification to a cumulus scheme, as listed in Table 2. The lateral and boundary conditions for the model are driven by the ERA5 reanalysis dataset, the fifth-generation reanalysis product of the European Center for Medium-Range Weather Forecasts, with a spatial resolution of 31 km [55]. The dataset is downloaded for a two-year period from January 01, 2018, to December 31, 2019.

3.2. Sensitivity analysis

For the calibration of physics parameterizations and setups, three sensitivity tests are carried out in the model calibration stage. The first test (T1) consists of six combinations for domain nesting options and nudging options for data assimilation. Domain nesting considers 1-way nesting with no interaction between outer and inner domains, and 2-way nesting enables domain interaction. For 1-way nesting, the boundary and lateral conditions are downscaled unidirectionally from the outermost domain to the innermost domain, whereas 2-way nesting enables feedback from the child domain to the parent domain, creating a bidirectional flow of downscaled data. Nudging is a parameter in the four-dimensional-data-assimilation method of WRF, and it enables use of the Newtonian relaxation term to closely retain the model outputs in reference to its driving or observed datasets over the run time [26]. There are three types of nudging in the WRF model: GN, SN, and observational nudging. The first two are studied in T1 with a nudging coefficient of 0.0003/s and are nudged above PBL. Moreover, the associated gridded nudging variables include V, T, and Q. Spectral nudging consists of wind components, potential temperature, and geopotential height.

The second test (T2) finds the most appropriate PBL scheme of the six PBL choices. Nonlocal schemes, such as Yonsei University (YSU) and Asymmetric Convective Model (ACM2) PBLs, and turbulent kinetic energy schemes [56], such as Mellor-Yamada-Janjic (MYJ), Quasi-Normal Scale Elimination (QNSE), Mellor-Yamada Nakanishi and Niino Level 2.5 (MYNN 2.5), and Bretherton and Park (UW) PBLs, are considered in the tests.

Finally, having fixed the settings for the parameters in T1 and T2, the nudged variable effects are investigated in the third test (T3). Table 3 provides a summary of the sensitivity test design.

All tests are run for 17 days from November 29, 2019 until December 15, 2019. The first two days are considered to be a spin-up period, in which the model reaches its atmospheric equilibrium state, and the spin-up period is discarded from the analysis. The simulated hourly wind vectors in D03 were retrieved from the nearest grid points to the four AWS locations prior to validation against their observed winds. The WRF performance is evaluated by statistical analyses and Taylor diagrams and can be found in the Supplementary Material.

3.3. Statistical metrics

The statistical indexes used for analysing the model performance are MBE, RMSE, STDE, and r , which are defined as follows:

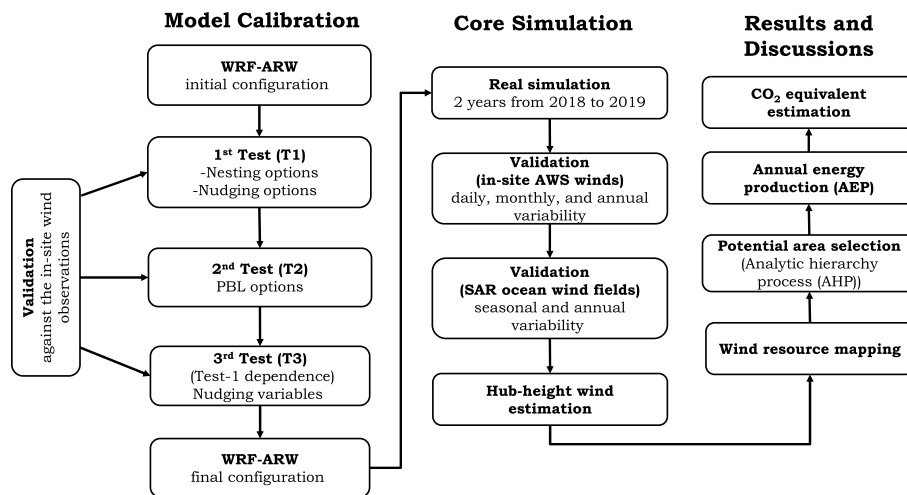


Fig. 3. Research flowchart consisting of two parts: model calibration and core simulation.

Table 2

WRF model setups and physics parameterizations determined from the sensitivity analysis.

Setup/parameterization	D01	D02	D03
Initial and boundary condition	ERA5 reanalysis		
Vertical layers	38		
Projection	Mercator		
SST update	Enabled		
Grid spacing	15 km	5 km	1.66 km
Domain size	180 × 190	277 × 289	298 × 298
PBL scheme	Yonsei University (YSU)		
Surface layer scheme	Revived Monin-Obukhov (Revised MM5)		
Land surface scheme	Unified Noah land surface layer		
Microphysics scheme	WRF Single-Moment 6-class (WSM6)		
Shortwave radiation scheme	Dudhia		
Longwave radiation scheme	RRTMG		
Cumulus scheme	Bett-Miller-Janjic (BMJ)		none

Table 3

Summary of WRF sensitivity tests with subdivided experiments. Bold indicates the resulting best option of the test. (1 = one-way nesting, 2 = two-way nesting, NN = no nudging, GN = gridded nudging, SN = spectral nudging, V = wind components, T = potential temperature, Q = water vapor mixing ratio, Re. = Revised).

Test	Experiments						
T1	<i>Nesting with nudging options</i>						
	1NN	1 GN	1SN	2NN	2 GN	2SN	
T2	<i>PBL options with respective surface layers</i>						
	YSU	MYJ	QNSE	MYNN2.5	ACM2	UW	
	Re.	Janjic	QNSE	MYNN	Re.	Re.	
	MM5	Eta			MM5	MM5	
T3	<i>Nudged variable options</i>						
	V	T	Q	VT	VQ	TQ	VTQ

$$MBE = \frac{1}{N} \sum_{i=1}^N (P_i - O_i) \quad (1)$$

$$RMSE = \sqrt{\frac{1}{N} \sum_{i=1}^N (P_i - O_i)^2} \quad (2)$$

$$STDE = \sqrt{\frac{1}{N} \sum_{i=1}^N \left((P_i - O_i) - \frac{1}{N} \sum_{i=1}^N (P_i - O_i) \right)^2} = \sqrt{RMSE^2 - MBE^2} \quad (3)$$

$$r = \frac{\sum_{i=1}^N (O_i - \bar{O})(P_i - \bar{P})}{\sqrt{\sum_{i=1}^N (O_i - \bar{O})^2 \sum_{i=1}^N (P_i - \bar{P})^2}} \quad (4)$$

where O_i and \bar{O} represent instantaneous and averaged values of the observed wind speed; P_i and \bar{P} represent instantaneous and averaged values of the modelled wind speed; and N is the number of samples matched in the computation.

For wind direction, the circular characteristics must be considered, and the formulas for MBE, RMSE, and STDE, based on [28,57], are given as follows:

$$MBE_{dir} = \frac{1}{N} \sum_{i=1}^N D_i \quad (5)$$

where D_i is determined by the following expressions:

$$\begin{aligned} &\text{If } P_{i,dir} < O_{i,dir}, D_i = P_{i,dir} - O_{i,dir} \text{ for } |P_{i,dir} - O_{i,dir}| < |360 + (P_{i,dir} - O_{i,dir})| \\ &D_i = 360 + (P_{i,dir} - O_{i,dir}) \text{ for } |P_{i,dir} - O_{i,dir}| > |360 + (P_{i,dir} - O_{i,dir})| \end{aligned} \quad (6)$$

$$\begin{aligned} &\text{If } P_{i,dir} > O_{i,dir}, D_i = P_{i,dir} - O_{i,dir} \text{ for } |P_{i,dir} - O_{i,dir}| < |(P_{i,dir} - O_{i,dir}) - 360| \\ &D_i = (P_{i,dir} - O_{i,dir}) - 360 \text{ for } |P_{i,dir} - O_{i,dir}| > |(P_{i,dir} - O_{i,dir}) - 360| \end{aligned} \quad (7)$$

where $P_{i,dir}$ and $O_{i,dir}$ are instantaneous modelled and observed direction values in degrees.

$$RMSE_{dir} = \sqrt{\frac{1}{N} \sum_{i=1}^N D_i^2} \quad (8)$$

$$STDE_{dir} = \sqrt{RMSE_{dir}^2 - MBE_{dir}^2} \quad (9)$$

In Eq. (8), D_i is computed by the following expression:

$$D_i = \min(|P_{i,dir} - O_{i,dir}|, |360 + (P_{i,dir} - O_{i,dir})|) \quad (10)$$

The MBE measures the model's overall tendency in reference to the in-situ data. A negative value means underestimation, whereas a positive value indicates overestimation. RMSE is a statistical tool determining the error intensity between the model output and the observed data. RMSE amplifies the impact of large errors on the results. STDE provides information about error dispersion and randomness. For r values ranging between -1 for a perfect negative correlation and $+1$ for a perfect positive correlation, STDE illustrates how well the two data fit

in a linear association.

3.4. Core simulation

After the model calibration through the sensitivity analysis, the WRF simulation over two years from January 2018 to December 2019 is carried out to consider the seasonal and annual variations in winds in the study region. Then, the downscaled two-year outputs are validated with the OWI data at a 10 m height.

The OWI wind data of the Sentinel-1 L2 OCN product needs to be preprocessed prior to comparison. First, the retrieved SAR images are

$$P(V) = \begin{cases} 0 & 0 \leq V \leq 3 \\ -5.937V^4 + 138.978V^3 - 953.975V^2 + 2936.464V - 3525.253 & 3 < V \leq 11 \\ -187.5V^2 + 4812.5V - 18875 & 11 < V \leq 13 \\ 12000 & 13 < V \leq 25 \\ 0 & V > 25 \end{cases} \quad (12)$$

$$P(V) = \begin{cases} 0 & 0 \leq V \leq 3.1 \\ -0.2946V^3 + 108.4055V^2 - 576.7256V + 755.9163 & 3.1 < V \leq 11 \\ -250V^2 + 6450V - 33600 & 11 < V \leq 13 \\ 8000 & 13 < V \leq 25 \\ 0 & V > 25 \end{cases} \quad (13)$$

$$P(V) = \begin{cases} 0 & 0 \leq V < 3 \\ 1.602V^3 + 18.536V^2 - 89.567V + 84.326 & 3 \leq V \leq 9.5 \\ 23.09V^3 - 891.58V^2 + 11453.04V - 45873.85 & 9.5 < V \leq 13 \\ 3075 & 13 < V \leq 25 \\ 0 & V > 25 \end{cases} \quad (14)$$

georeferenced to their remotely sensed coordinates. Then, the images are resampled using the nearest neighbour technique to align the raster cells. Furthermore, SAR wind is ENW at 10 m ASL. As the deviation between the wind speed at the neutral state and at atmospheric stratification appears to be small (≤ 0.5 m/s) over the ocean surface and has a long coverage period, it could be assumed that the mean atmospheric stability becomes similar to the neutral state [58]. Hence, a direct comparison can be made. Since WRF has generated hourly wind fields and the OWI winds are not periodically hourly, the temporal collocation between the two is made 30 min before or after the WRF data time. Consequently, between 2018 and 2019, 515 SAR scenes from both Sentinel-1A and 1B were temporally collocated with 289 WRF rasters in D03. Spatially, the WRF images whose grid spaces are approximately $1.66 \text{ km} \times 1.66 \text{ km}$ are internally regressed to approximately $1 \text{ km} \times 1 \text{ km}$, which is the horizontal resolution of the SAR images.

3.5. Wind power density

Wind power density (WPD) is the theoretical amount of power per unit of a wind turbine rotor's sweeping area generated at a given wind speed and defined by the following equation:

$$\frac{P}{A} = \frac{1}{2} \rho V^3 \quad (11)$$

where ρ is an air density of 1.225 kg/m^3 and V is the wind speed at a particular time. Regarding the calculation of the mean WPD, rather than applying a mean wind speed to Eq. (11), the average instantaneous WPD originating from the instantaneous wind speed is computed to improve the result.

3.6. Turbine-generated wind power and capacity factor

Practically, the wind power is calculated at the hub height. Three offshore wind turbine models are selected, Vestas V112, Vestas V164, and GE Haliade-X (HX12), having rated powers of 3 MW, 8 MW, and 12 MW, respectively. The features of the turbines are listed in Table A1.

The turbine power curves obtained from Refs. [59,60] are shown in Fig. A1. The curve functions are approximated using polynomial regression. For HX12, the curve is represented by Eq. (12) and the curves of V164 as well as V112 are expressed by Eq. (13) and Eq. (14).

The average power (\bar{P}) generated from the turbines whose curve is $P(V)$ under a wind regime described by a Weibull probability distribution function $f(V)$ can be calculated using the following equation:

$$\bar{P} = \int_0^\infty P(V)f(V)dV \quad (15)$$

To determine $f(V)$, hourly wind speed results for 2 years from WRF modelling are converted into raster format and then the scale and shape parameters for $f(V)$ are calculated for each cell in the EEZ. The capacity factor (CF) is a key indicator of the turbine's ability to convert wind power at the erection site. This factor is expressed by a ratio between an average power produced by the turbine (\bar{P}) and the rated power of the turbine (P_r) over time [61]:

$$CF = \frac{\bar{P}}{P_r} \quad (16)$$

3.7. Site suitability

To define the suitable siting of the turbines, a multicriteria decision-making method is utilized [18,19]. Three factors are considered: WPD, bathymetry, and distance from shore. Other factors, such as the marine environment, tourism, disturbances to living activities and business, are also important, but they are out of the study scope.

To perform the task, the weighted overlay tool in ArcGIS is selected. The WPD is categorized based on the wind power classes developed by Refs. [62,63] at 50 m (Table 4). The bathymetry is classified on the basis of turbine foundations [8,9], as shown in Table 5. For distance to shore, two scenarios are considered (Table 6): the first scenario is that 15 km from the shore is excluded because it is reserved for near-coast activities

Table 4

Classification of wind power density and resource potential assessment.

Wind Power Classes	Suitable index (SI)	Resource Potential	10 m AGL		50 m AGL	
			WPD (W/m ²)	Wind Speed (m/s)	WPD (W/m ²)	Wind Speed (m/s)
1	1	Poor	0–100	0–4.4	0–200	0–5.6
2	2	Marginal	100–150	4.4–5.1	200–300	5.6–6.4
3	3	Fair	150–200	5.1–5.6	300–400	6.4–7.0
4	4	Good	200–250	5.6–6.0	400–500	7.0–7.5
5	5	Excellent	250–300	6.0–6.4	500–600	7.5–8.0
6	6	Outstanding	300–400	6.4–7.0	600–800	8.0–8.8
7	7	Superb	400–1000	7.0–9.4	800–2000	8.8–11.9

Table 5

Types of turbine foundations in relation to their applicable sea depths.

Foundation types	Sea depth (m)	SI
Monopile	0–35	7
Lattice monopile	35–50	6
Tripod/Jacket	50–100	5
Floating	100–1000	4

Table 6

Classification of distance intervals off the coast.

First scenario		Second scenario	
Distance to shore (km)	SI	Distance to shore (km)	SI
≤15	(excluded)	0–20	7
15–20	7	20–30	6
20–30	6	30–40	5
30–40	5	40–50	4
40–50	4	50–60	3
50–60	3	60–70	2
60–70	2	70–80	1
70–80	1	≥80	1
≥80	1		

and avoidance of visual focus [64]. After 20 km, the 10-km interval is applied up to 80 km away. The second one is that no offset is made for nearshore area. Then, a common 1–7 scale is assigned to each class for the three factors. The scale is called a suitable index (SI), indicating the level of suitability from least (1) to most (7). The weights given to the three factors are determined by the analytic hierarchy process (AHP).

3.8. Annual energy production and CO₂ emission equivalent calculation

After locating the optimal siting for turbines, the total number of turbines to be installed can be computed as follows:

$$N_t = \frac{S}{AS} \quad (17)$$

where S is the total potential surface area in km², and AS is the array spacing of a turbine in km². According to Ref. [9], the optimized spacing for each individual turbine is defined as follows:

$$AS = D^2 \times DSF \times CSF \quad (18)$$

in which D is the rotor diameter in metres; DSF , the downwind spacing factor, equals 10; and CSF , the crosswind spacing factor, is 5.

The mean annual energy production (AEP) is the average energy generated by the turbines within a year. To account for the effects of wake loss and operation time of a hypothetical wind farm, the simplified form of the AEP expression in Ref. [5] can be written as follows:

$$E_y = (1 - L_w) \times C_A \times P_r \times N_t \times CF \times 8760 \quad (19)$$

where L_w is the wake loss rate, assumed to be 10% [65], and C_A is the availability coefficient, assumed to be 95% [9].

The CO₂ equivalent amount of the AEP is determined as follows:

$$EM = E_y \times CM \quad (20)$$

The combined margin (CM) in an electricity system is the summation of the weighted averages of the operating power plant emission factors (operation margin (OM)) and prospective power plant emission factors (build margin (BM)) [66]. In Cambodia, based on [67], the CM was found to be 0.4588 t-CO₂/MWh for the national grid with weights of 25% and 75% for the OM and BM, respectively.

4. Results

4.1. Calibration

4.1.1. Sensitivity test 1 (T1): nesting and nudging options

The time-series comparison between the observed and modelled wind speeds at the four AWSs is shown in Fig. S2. Overall, all experiments could capture the variation in the in-situ wind speed at KP, KPS, and TK, except at KK. However, they appeared to overestimate the observed wind speed at all stations. Among the experiments, 1 GN and 2 GN showed similar MBE and RMSE values but were higher than the rest. In addition, their STDE and r values were the best at most of the stations (Table S1). In contrast, 1NN depicted the best MBE and RMSE but did not perform well in terms of the STDE and r value. Notably, nesting options may not have a significant effect on the results even though they were tested in combination with nudging options. As none of the experiments were best for the four statistical metrics, the Taylor diagrams in Fig. S3 were used to determine the optimal choice. As a result, 2 GN likely led other experiments at KP, KPS, and TK. At KK, the best performance belonged to 2NN. Furthermore, 1SN was the worst experiment at almost all stations.

For wind direction, the experiments underestimated the in-situ data at all stations. There was no noticeable difference among the experiments, yet among the stations, KP had the largest MBE and STDE (>100°). Moreover, it was difficult to select the best experiment, as the results seemed to be more site-specific: best STDE at KP and KK was 2SN; at KPS, it was 2NN; and at TK, it was 1SN (Table S2). Since the aim was to create a wind resource map, priority was given to the wind speed outcomes; therefore, it could be concluded that 2 GN was the optimal setting for the nesting and nudging options in test 1 (T1).

4.1.2. Sensitivity test 2 (T2): planetary boundary layer schemes

The six PBL time series in T2 are displayed along with the observed time series at the four sites in Fig. S4. All experiments reproduced the in-situ wind speed patterns well at all stations despite the overall positive bias. In particular, the MYJ and QNSE PBLs likely produced the highest overreaches during the daytime at all AWSs. This feature was statistically reflected by the largest magnitudes of MBE, RMSE, and STDE of the schemes in Table S3. Moreover, the MYNN2.5 PBL had the lowest MBE and RMSE and highest correlation values at most of the sites. Additionally, the YSU scheme, whose performance was optimal in global simulations [24], earned the best STDE values at KP, KPS, and TK. The Taylor diagrams in Fig. S5 apparently confirmed that the QNSE PBL

performed poorly at all stations and that the second worse PBL scheme could be the MYJ. Furthermore, the MYNN2.5 option slightly led others at KK and TK and was the second-best scheme at KP after ACM2. At KPS, the best scheme was the YSU PBL.

In terms of wind direction, the errors were similar to the T1 outcomes, possibly meaning that all PBL options did not vary the model's ability to predict wind direction (Table S4). Therefore, the MYNN2.5 scheme was concluded to be the most suitable for this study.

4.1.3. Sensitivity test 3 (T3): nudged variables

In this test, seven experiments of nudged variables were examined. Fig. S6 demonstrates that the observed wind speed pattern could be reproduced by all experiments. Nevertheless, the overall tendency for overestimation exists. Based on Table S5 and Table S6, for wind direction, no experiments exhibited outstanding performances concerning the four metrics. The nudged variable options might not impact the WRF model's prediction behaviour. However, for wind speed, nudging T led to the lowest MBE and RMSE, whereas nudging V seemed to result in the smallest STDE values. The best r values arose when VT and VTQ were nudged. Based on the Taylor diagrams in Fig. S7, the nudged V was the leading experiment at KK and TK, although its deviation from others was only marginal. At KP, the optimal choice was nudging VQ followed by

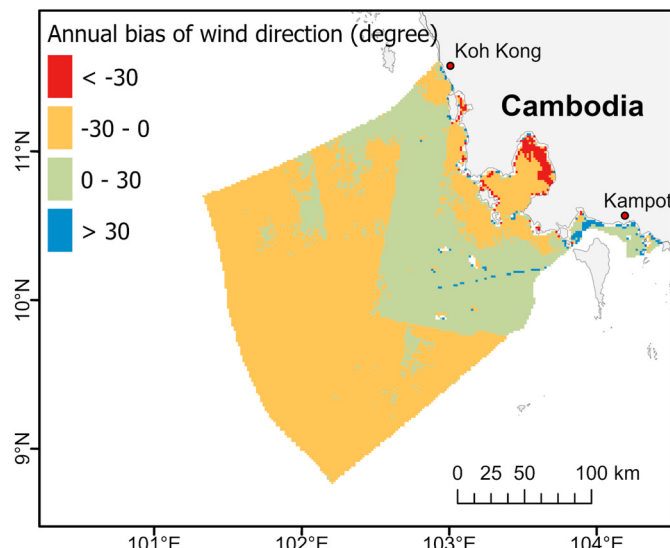
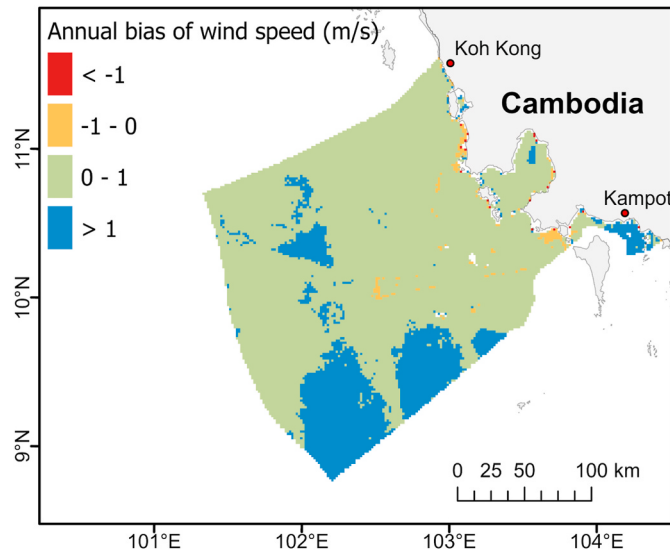


Fig. 4. Spatial distribution of annual mean bias of wind speed and wind direction between the WRF results and the SAR winds over the EEZ at 10 m ASL.

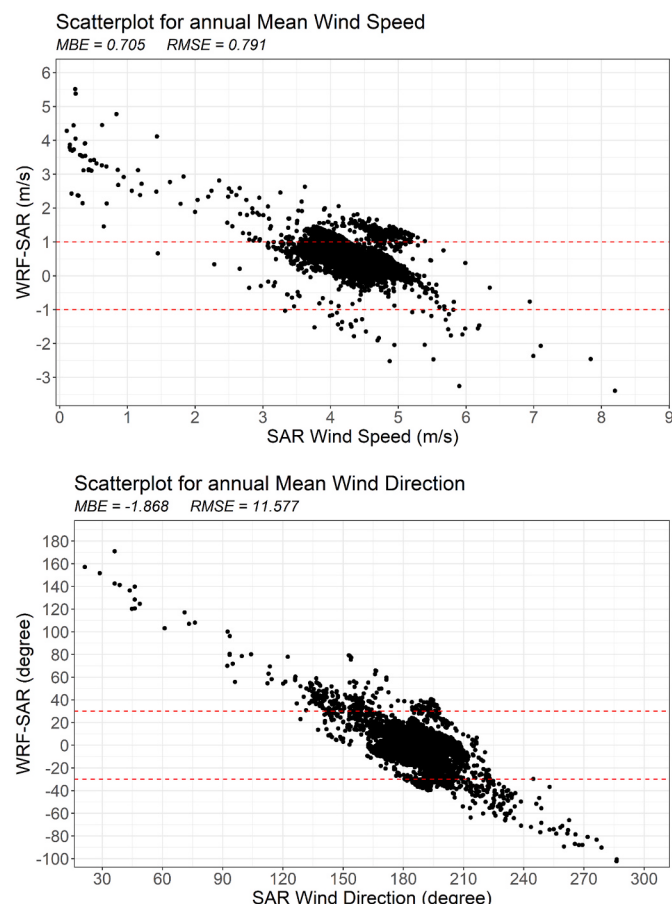


Fig. 5. Scatterplots between the annual mean bias error (MBE) of wind speed and SAR wind speed and between the annual MBE of wind direction and SAR wind direction over the EEZ at 10 m ASL.

nudging V and VTQ. The nudged T was the best option at KPS, followed by the TQ experiment. With these results, nudging V was chosen from the optimal configuration test for the nudging variable option.

4.2. Validation with the OWI wind data

In Fig. 4, the WRF versus SAR wind speed comparison culminated in the annual MBE of between -1 m/s and 1 m/s , covering most of the EEZ. WRF mostly overestimated the SAR except in a few areas, especially near shore. The spatial average annual MBE was 0.70 m/s , and the RMSE was 0.79 m/s (Fig. 5), indicating that the two datasets agreed well. Notably, SAR wind speeds between 3 and 5 m/s could be well predicted by WRF. The errors apparently grew larger when the SAR wind speed was outside this range. Additionally, an absolute MBE greater than 1.5 m/s likely occurred close to the shore, probably due to the SAR quality affected by nearshore activities or land-sea masks.

For wind direction, the WRF slightly underestimated the SAR ($-30\text{--}0^\circ$). As depicted in Fig. 5, the spatial average of the annual MBE was as small as -1.86° , and the RMSE was 11.57° , meaning that WRF could capture the SAR wind direction very well. The predominant wind direction was from the south. Based on the results, the WRF model could be used for wind resource mapping in offshore areas of Cambodia.

4.3. Seasonal wind variability

The MBE in March-April-May (MAM) was much lower than that in the rest of the year (between -1 m/s and 1 m/s), and the best reproduction of SAR wind speed was achieved by WRF (Fig. 6). The errors were larger in September-October-November (SON) and June-July.

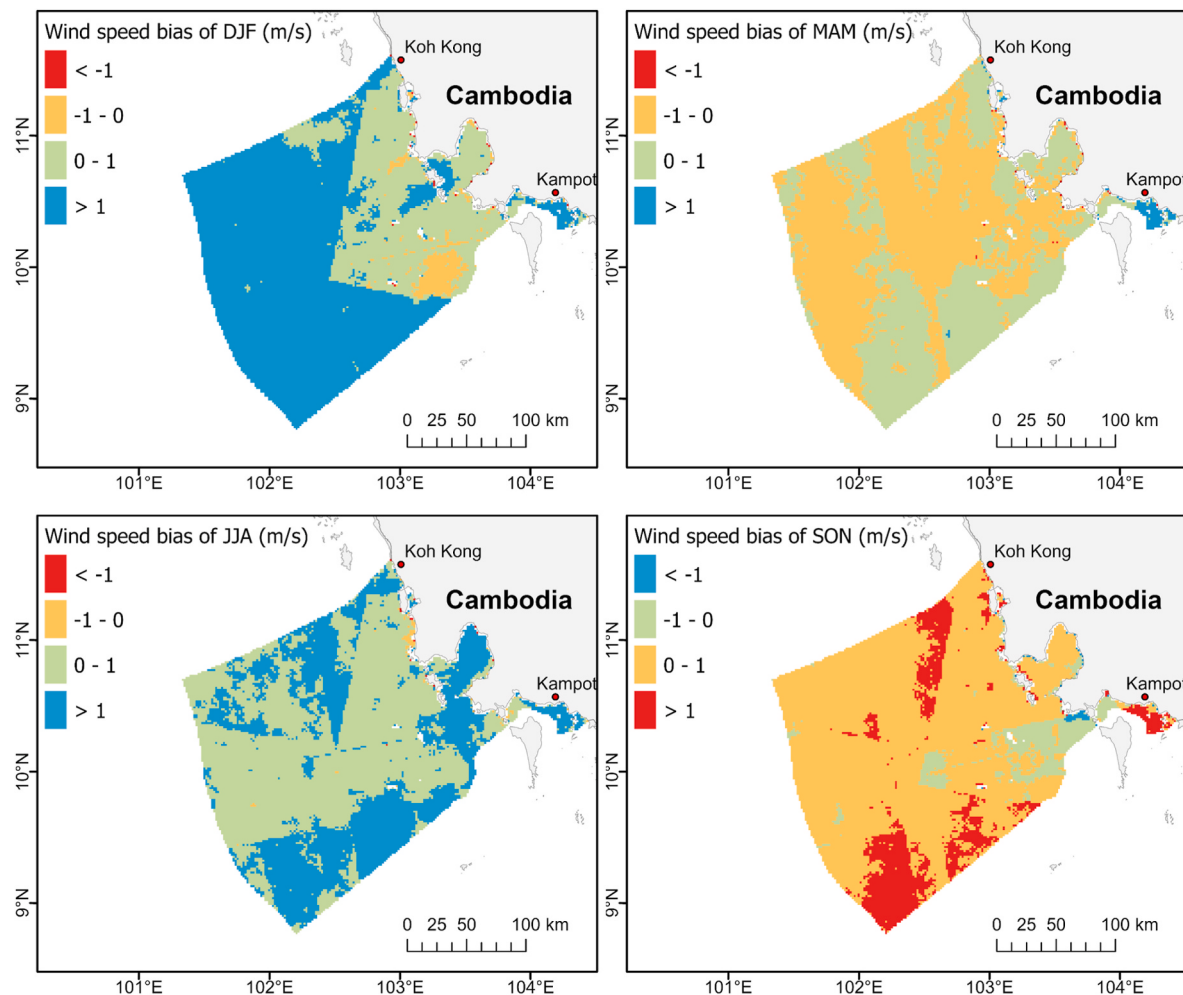


Fig. 6. Seasonal variability in the MBE between the WRF and SAR wind speeds.

August (JJA). In December-January-February (DJF), the WRF prediction seemed worst among other periods because an MBE greater than 1 m/s covered more than half of the EEZ. Because of the monsoon influence over Cambodia, DJF and JJA are periods of stronger wind. Moreover, the low SAR samples for each season likely contribute to the errors.

Fig. 7 shows that the SAR wind direction could be well predicted by WRF in all seasons. Notably, both datasets agreed on the south being the predominant wind direction in SON, the west-southwest in JJA, and the east-southeast in DJF. In MAM, despite a slight deviation, it was sufficiently correct to mention around the south. The findings in JJA and SON were in line with the nominal southwestern wind of the monsoon during these months. However, the resulting directions of DJF and MAM apparently shifted from the typical northeastern direction of the monsoon wind during this period.

4.4. Wind resource mapping

To estimate the wind resources, interpolated wind outputs from postprocessing were retrieved at three heights: 80 m, 100 m, and 140 m ASL. In Fig. 8, the dominant annual mean wind speed at both levels was between 5 m/s and 6 m/s. The spatial averages of the annual mean wind speeds of 5.15 m/s, 5.20 m/s, and 5.27 m/s were found at heights of 80 m, 100 m, and 140 m, respectively. Remarkably, the strongest wind speeds of 6–7.22 m/s at 80 m ASL, 6–7.45 m/s at 100 m ASL, and 6–7.62 m/s at 140 m ASL occurred in the sea along the coastline of the Kampot and Kep Provinces. The predominant annual mean wind direction at all

heights was from the south. It might be concluded that the annual mean wind speed and direction over the EEZ did not significantly change with the low vertical levels.

Fig. 9 illustrates the spatial distribution of the annual mean WPD. The spatial average was estimated to be 188.75 W/m² at 80 m ASL. It increased to 197.68 W/m² at 100 m ASL and 207.89 W/m² at 140 m ASL. The highest WPD (>300 W/m²) was concentrated along the coast of the Kampot Province at 80 m ASL and extended further east, reaching the Kep coastline at 100 m and 140 m ASL. The maximum annual mean WPD reached 540.26 W/m². In the GoT area, according to the wind power classes (Table 4) developed in Refs. [62,63], the estimation apparently ranged from poor (<200 W/m²) to good (400–500 W/m²) WPD at all heights. Thus, the Cambodian EEZ has promising potential for offshore wind development, especially along the Kampot and Kep shorelines.

4.5. Wind power and capacity factor

The annual mean wind power outputs of the turbines at 80 m, 100 m, and 140 m ASL for each pixel are illustrated in Fig. 10. The averaged power seemed to increase twice as the hub height grew from 80 m to 100 m and fourfold from 80 m to 140 m, which might be because of the higher rated power of V164 (8 MW) and XH12 (12 MW) relative to V112 (3 MW). Consequently, a slight increase in wind speed could culminate in considerable power production. The power distribution reached a maximum of 1226.78 kW at 80 m, 2969.77 kW at 100 m, and 5181.60

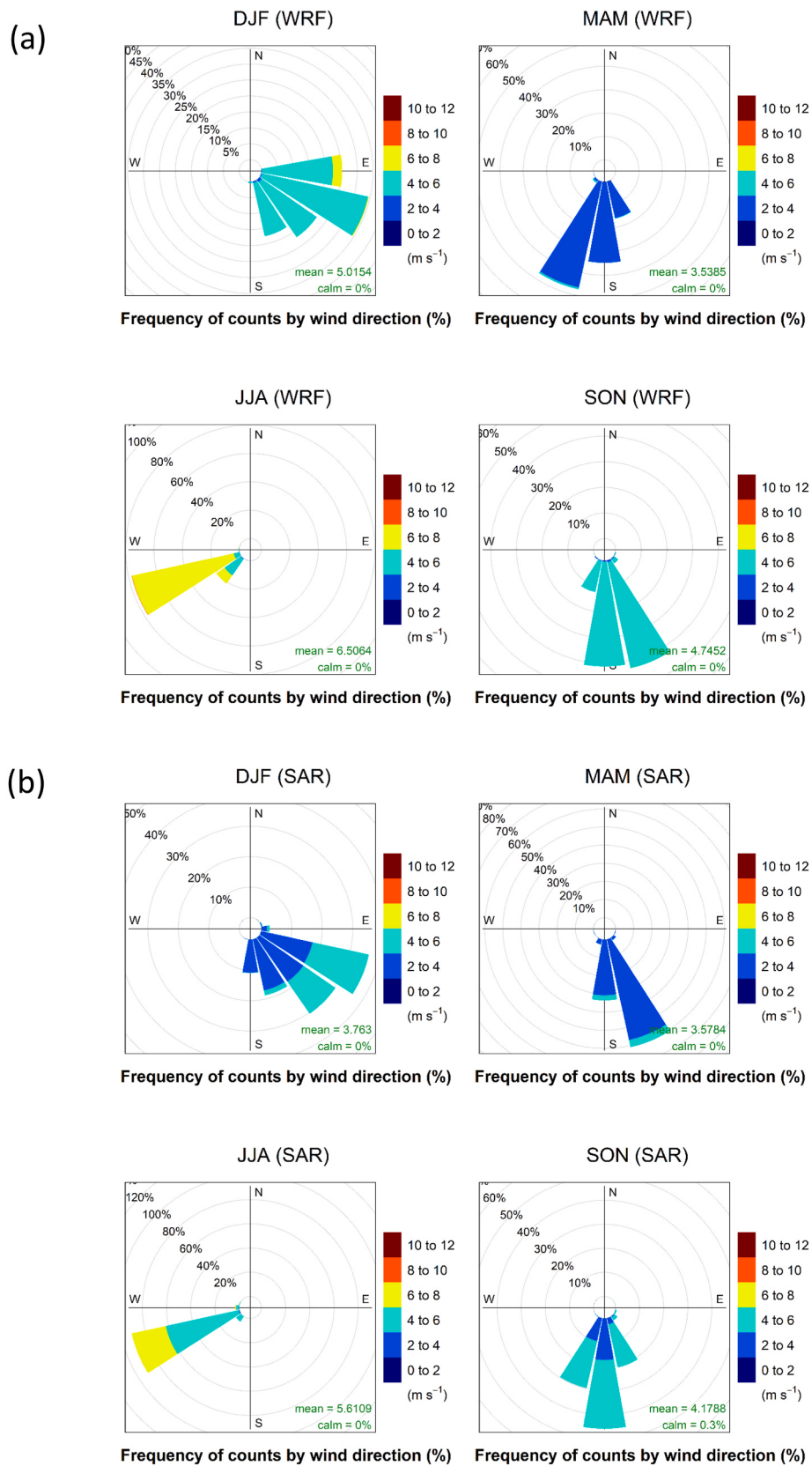


Fig. 7. Wind roses depicting seasonal variability in winds from (a) the WRF results and (b) SAR data.

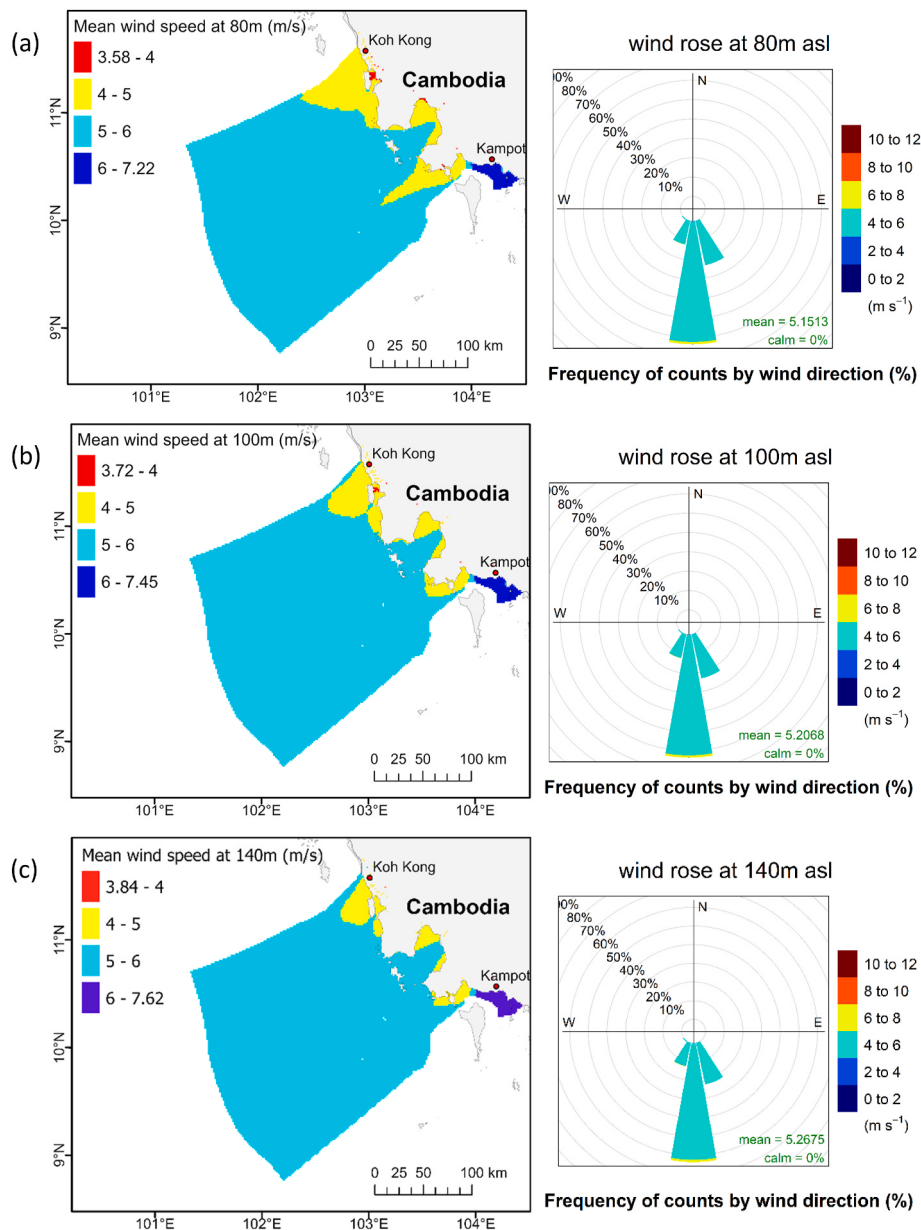


Fig. 8. The spatial distribution of annual mean wind speed generated by the WRF model at (a) 80 m, (b) 100 m, (c) 140 m height ASL and their respective wind roses.

kW at 140 m in areas along the coastline of the Kampot and Kep Provinces, but the other nearshore portions exhibited the least power. The rest of the EEZ was largely covered by moderate outputs.

The spatial distribution of CF calculated by Eq. (16) are shown in Fig. 11. The CF ranges of V112 and V164 in the study area were quite similar but notably expanded to 0.43 with HX12. The spatially averaged CF for the whole EEZ at 80 m was 0.21, while those at 100 m and 140 m were 0.18 and 0.22.

4.6. Annual energy production and CO₂ emission equivalent

To estimate the AEP, the suitable farm sites need to be defined as described in Section 3.7. Table 7 shows the pairwise matrix setup used in the AHP [68–72]. From the matrix, the weight coefficients (priority values) of the three factors could be determined with a consistency ratio of 0.006, which was much smaller than 0.1, indicating that the weights found here were reasonably consistent and applicable for the study.

The threshold value for the optimal sites was determined by summation of the weighted SI for WPD (300–400 W/m²), bathymetry

(deeper than 50 m below the surface), and distance from the shore (40 km–50 km). As a result, a value of 3.42 became the threshold value. Thus, the areas marked by an index greater than or equal to 4 in Fig. 12 and Fig. 13 were chosen for siting the turbines.

In the first scenario, the size of the optimal areas was estimated to be 109.98 km² at 80 m ASL, and it stretched further to cover 241.96 km² at 100 m ASL and 503.17 km² at 140 m ASL. The corresponding spatial averages of the CF were 0.23, 0.19, 0.22 for V112, V164, and HX12, respectively (Table 8). In addition, the spatial arrangement of turbines specified in Section 3.8 yielded a total number of 175 for the V112 turbine, 180 for the V164 turbine, and 207 for the HX12 turbines over all optimal areas. The estimation of the total AEP at 80 m, 100 m, 140 m was 927.00 GWh, 2049.20 GWh, and 4268.28 GWh, which could help reduce the amount of CO₂ emissions by 0.42 Mt-CO₂, 0.94 Mt-CO₂, 1.96 Mt-CO₂ per year, respectively.

In the second scenario (Table 9), it could be seen that the potential areas grew over 6 times of those in the first 15 km-offset scenario, reaching 1198.82 km² at 80 m ASL, 2029.20 km² at 100 m ASL, 3423.26 km² at 140 m ASL after excluding two marine protective zones: Koh

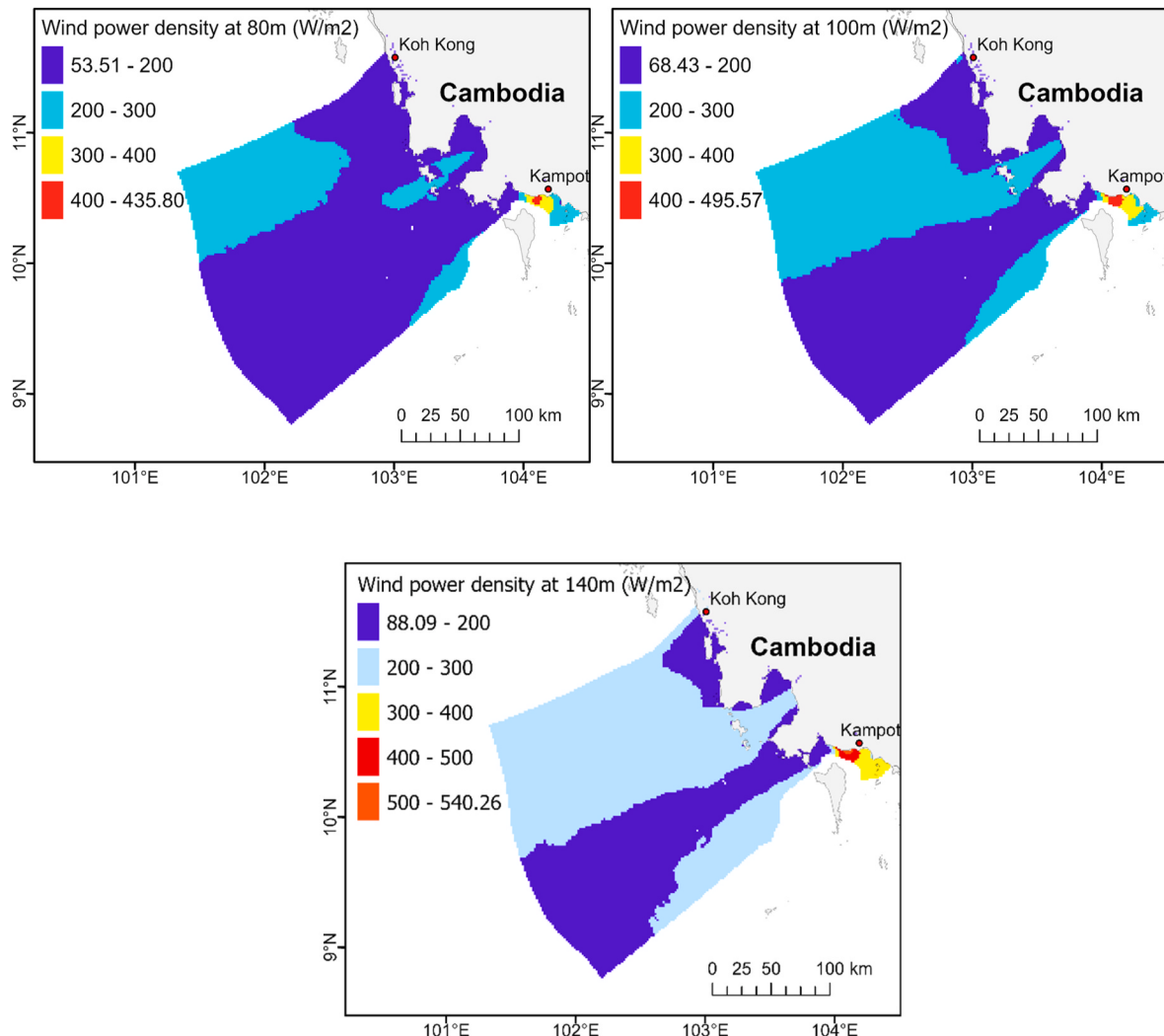


Fig. 9. The spatial distribution of the wind power density (WPD) over the EEZ at 80 m, 100 m, and 140 m ASL.

Rung Marine National Park and Ream National Park. The number of turbines distributed across the optimal areas was estimated to be 1911 for V112, 1509 for V164, and 1415 for HX12 generating considerable AEP of 11,949.20 GWh, 20,013.34 GWh, and 31,880.48 GWh, respectively. Furthermore, the amount of CO₂ could be greatly reduced annually by 5.48 Mt-CO₂ for 80 m height, 9.18 Mt-CO₂ for 100 m height, and 14.63 Mt-CO₂ for 140 m height.

4.7. Impacts on future electricity

In the first scenario, the total AEP of 4268.28 GWh should be sufficient for supplying up to 34% of the country's demands for electricity in 2020. Unfortunately, it would take decades for projects and construction to obtain this amount of offshore wind energy. Therefore, it was assumed that 10% of the total AEP could be installed in the potential areas by 2030, which would be equivalent to 92.70 GWh for V112 (case 1), 204.92 GWh for V164 (case 2), 426.82 GWh for HX12 (case 3).

In case 1, the offshore wind source would be capable of supplying up to 1.94% (or 69,617) of total residential households in 2020 since an annual mean of energy consumption per residential household in Cambodia was estimated to be 1331.57 kWh based on [42]. Furthermore, it would contribute to approximately 0.15% of the total energy demand projected in 2030. In case 2, source generation would grow to

4.28% (or 153,893) of the total residential households in 2020, and its energy share in the system would expand to 0.33% in 2030. In the last case, the supply would further increase to 8.92% (or 320,543) of the total residential households in 2020 as well as 0.69% for projected energy share in 2030.

In the second scenario, by keeping the same assumption that 10% of the total AEP could be generated by the year 2030, the produced energy would be 1194.90 GWh, 2001.33 GWh, and 3188.04 GWh for 80 m (case 1), 100 m (case 2), and 140 m (case 3) height, respectively. For case 1, the number of residential households to be supplied rose from 1.94% in the first scenario to 25% (897,356) of the 2020 residential household record. In 2030, this 10% of the total AEP would make up 1.95% of the projected demand of the national grid. For case 2, the offshore source would increase from 4.28% in the first scenario to 41.86% (or 1,502,978) of the total residential households in 2020, and its energy share in the system would expand to 3.27% in 2030. For the case 3, the source would contribute to the supply of 66.69% (or 2,394,186) of the total residential households in 2020, and its energy share in the system would expand to 5.20% in the projected year 2030. These results pointed out that the offshore wind could make up a significant share of clean energy in Cambodian power system when a full uptake of the source potential could be achieved.

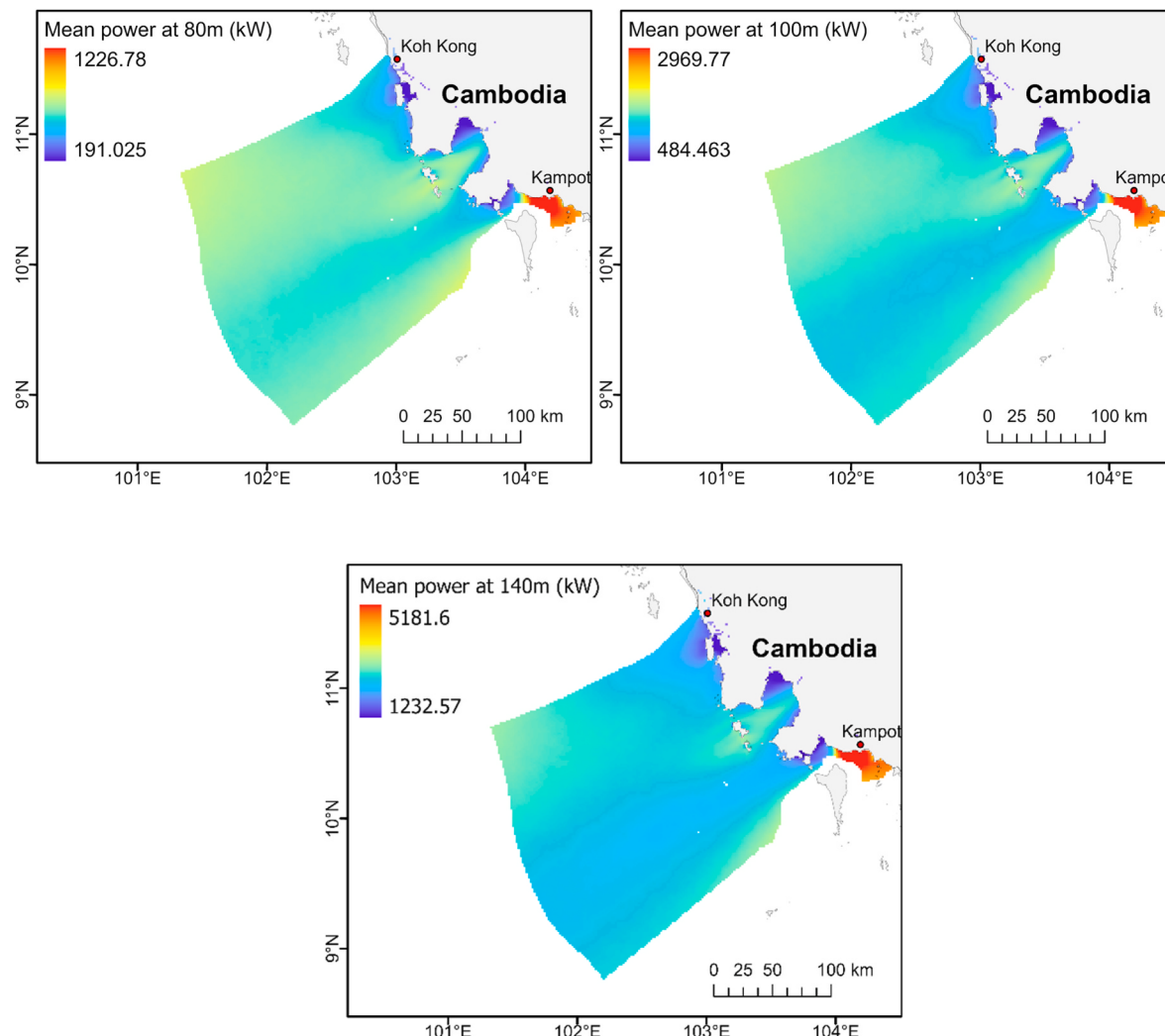


Fig. 10. The spatial distribution of the averaged power over the EEZ, generated by the V112 wind turbine at 80 m ASL, the V164 wind turbine at 100 m ASL, and HX12 wind turbine at 140 m ASL.

5. Discussion

5.1. Wind speed error

Through various tests of the WRF model's sensitivity, WRF seemingly overpredicted the onshore in situ wind speed at all stations at 10 m AGL. This tendency was also reported by Refs. [23,29,73]. Carvalho et al. [73] offered a sensible cause stemming from the WRF misrepresentation of the real topography in the valleys and at mountain tops. The elevation difference at the four AWSs between the default USGS GTOPO30 topographic data for WRF and the SRTM elevation data is investigated and presented in Table 1. The deviations at KP (3.16 m) and KK (15.03 m) are larger than the other two and correspond to larger errors of MBE and RMSE in the three sensitivity tests. The real topography of the KK and KP is complex and may contribute to bias and uncertainty even with a 1.66 km resolution. Another possible reason could be the lower amount of observed data assimilated in the reanalysis for the Cambodian region since the richness of the spatial wind distribution input over a particular area would improve the estimation quality of the reanalysis over that location. However, the offshore wind estimation over the EEZ of Cambodia with WRF illustrates satisfying results, as described in Sections 4.2–4.4.

5.2. Wind direction error

For the onshore wind direction, the RMSE values found in each test were significantly large ($>80^\circ$) at all stations. More noticeably, both the MBE and RMSE values at KP were more than one quadrant, while the MBE at the remaining stations was larger than -40° in all tests. However, when compared with the offshore SAR wind direction, the MBE and RMSE values of the WRF showed much better agreement. As pointed out in Refs. [74,75], the wind direction was affected more by the topographical representation in the model than the physical parameterizations, which could explain the difference between onshore and offshore validation of the wind direction despite their different lengths of time for the validations. Thus, the modelled wind direction accuracy could be improved when input data associated with topography, such as surface roughness, land use and land cover, geographical data, become more realistic at a fine resolution. In addition, further investigation should be conducted in future studies concerning how the wind direction was measured on onshore sites to verify their quality in Cambodia.

5.3. WRF accuracy versus SAR accuracy

The studies of De Montera et al. [38] and Hadjipetrou et al. [39], which validated the Sentinel-1 LN wind data against in situ buoys and stations, obtained annual mean biases of -0.4 m/s together with RMSEs

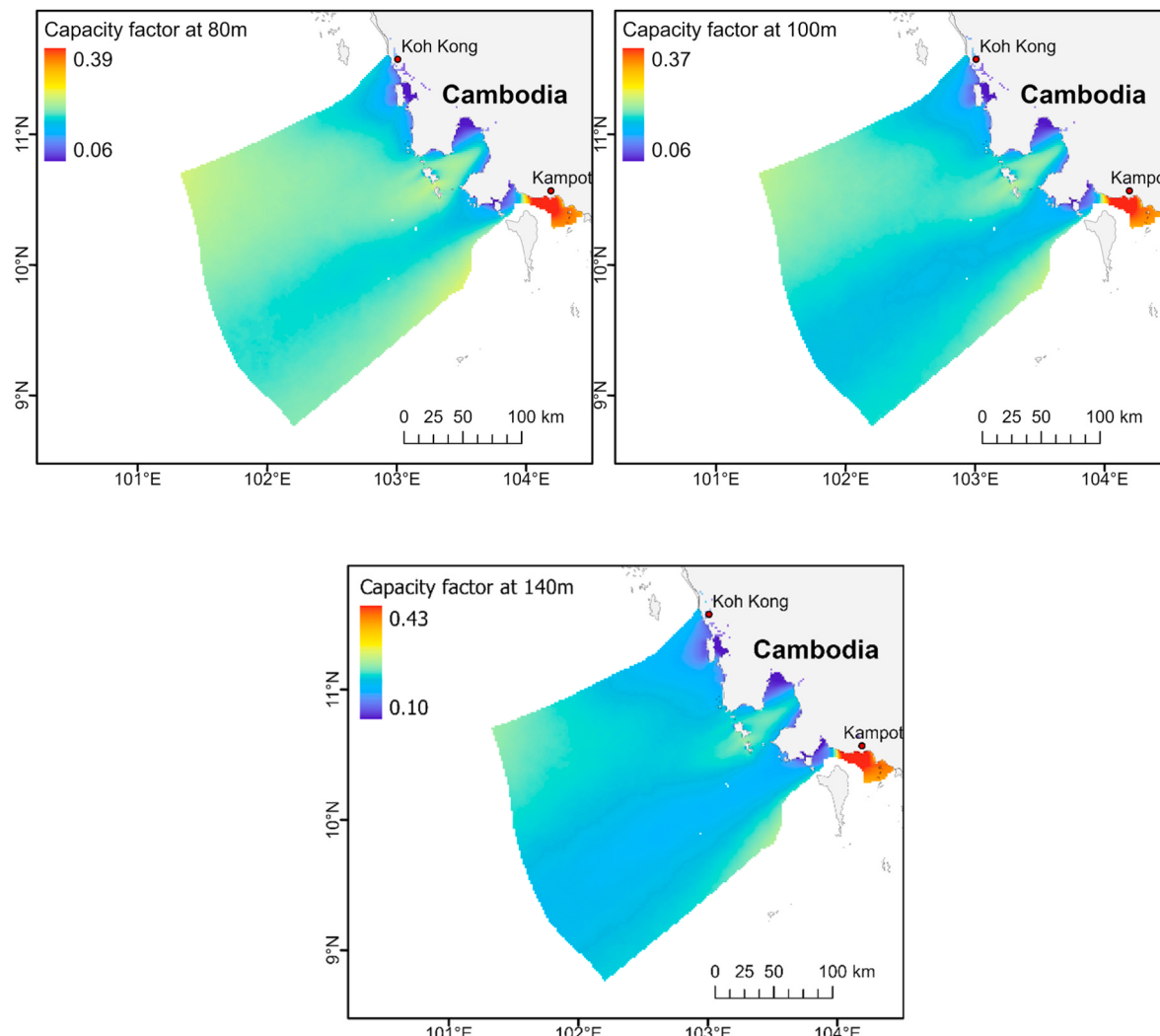


Fig. 11. The spatial distribution of CF over the EEZ, belonging to the V112 turbine at 80 m ASL, the V164 turbine at 100 m ASL, and the HX12 turbine at 140 m ASL.

Table 7

Pairwise matrix and consistency ratio determined in AHP (Bath. = bathymetry, D = distance, CI = consistency index, RI = random index, CR = consistency ratio).

	WPD	Bath.	D to shore	$\sqrt[n]{\text{product values}}$	Priority values	CI	RI	CR
WPD	1	7	3	2.75	0.67	0.003	0.58	0.006
Bathy	1/7	1	1/3	0.36	0.09			
D to shore	1/3	3	1	1.00	0.24			
Total				4.12				

of 1.45 m/s and 0.7 m/s, respectively. The present work validating the WRF wind data versus the same SAR dataset obtained a spatial average annual MBE of 0.70 m/s and RMSE of 0.79 m/s. Thus, the long-term wind velocity hindcast with WRF is sufficiently good for wind resource estimation where there is no offshore measurement. The results were likely better than the comparison between the WRF and QuickSCAT (mean bias of 0.84 m/s) in the region by Ref. [17]. Nevertheless, Barthelmie & Pryor [76] suggested that the mean wind speed and Weibull's scale parameter approximation could be obtained with 60–70 SAR images. They added that a variance computation could be conducted with approximately 150 scenes, whereas 2000 SAR scenes could be used to approximate the wind energy density or Weibull shape parameter. Due to the spatially dependent inadequacy of the SAR images in the present work, more SAR data should be collected for future research so that the errors might be improved.

5.4. Turbine choice

Based on the results in Section 4.4, the annual mean wind speed over the EEZ slowly grew from 100 m to 140 m height ASL. Even at 150 m height ASL, the spatial average of the mean wind speed for the three windiest months (June, July, and August) of 2019 increased just 0.4% from that at 140 m (Table 10), which could be concluded that the annual mean wind speed at the turbine height of 150 m ASL would narrowly deviated from that at 140 m ASL. Furthermore, the HX12 turbine is one of the latest technologies in the present market, and its higher rated power would extend the analysis range. Thus, the use of the HX12 might not affect the estimation of the wind resource at 140 m height ASL. The comparison results for the mean wind speed for each month between 140 m and 150 m heights and their spatial distribution over the EEZ can be found in the **Supplementary Material**.

Notably, the power outputs of V164 seem to be double those of V112

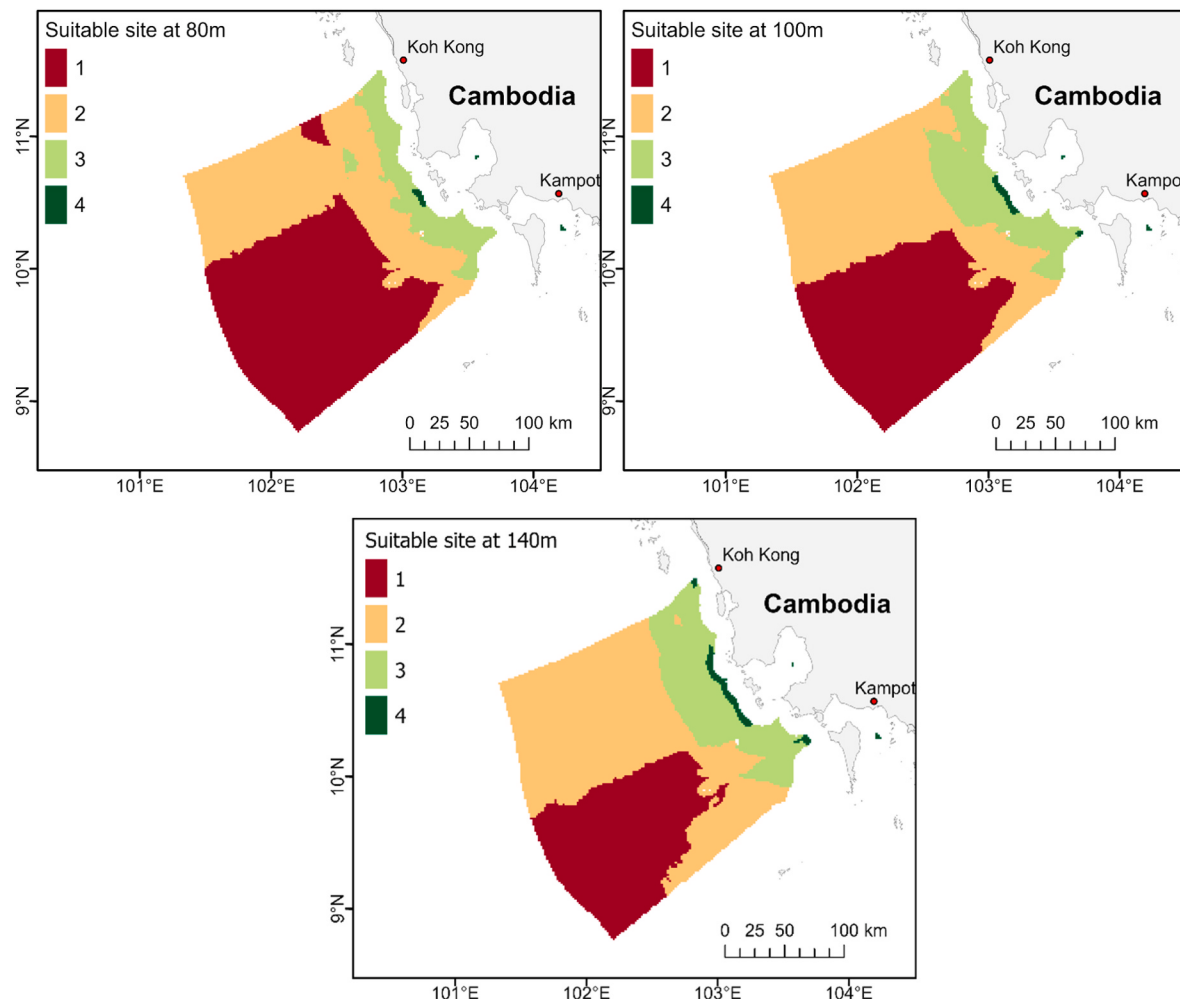


Fig. 12. The indexes marking the levels of suitability for an offshore wind farm within the EEZ at 80 m, 100 m, and 140 m ASL for the first scenario. A distance of 15 km offshore was excluded for nearshore activities and avoidance of visual disturbances. Level 4 is suitable for offshore wind farms.

as the hub height grows by 20 m. Moreover, as the height difference was 60 m, the power generated by HX12 becomes four times that of V112. Even though the average wind speed does not increase much with the heights in the EEZ, the steeper slope of the HX12 and V164 turbine power curves significantly influences the wide output difference. The better choice of a turbine for low WPD areas, such as the Cambodian EEZ, is a turbine with a taller hub height and higher rated power. However, according to Ref. [77], the CF of a turbine should be at least 25% and 30% because of the economic factors entailing more installation and maintenance costs in offshore projects. The HX12 and V112 appears to be closer to the recommended values. Thus, the final optimal turbine choice requires both technical and economic considerations in which the latter is beyond the scope of the present study. In addition, more studies are recommended for economic and environmental assessments of offshore projects in the Cambodian EEZ.

6. Conclusion

The objectives of the present study are to assess and create an offshore wind resource map in Cambodia with the

WRF model and Sentinel-1 L2 OCN imagery and to assess the AEP and CO₂ reduction amount. The sensitivity tests of WRF led to selection of the optimal settings: two-way nesting combined with gridded nudging, MYNN2.5 PBL scheme, and wind components for the nudged variable. In addition, the nesting choices likely had nonsignificant effects on the model performance. Another finding was that the wind direction was probably insensitive to all three tested parameters regardless of the stations.

After the model calibration and the long-term two-year simulation, the WRF wind fields showed satisfactory agreement with those from the SAR despite its slightly low accuracy in DJF and JJA, which could be caused by low sample numbers. Furthermore, the wind direction seen by both datasets in DJF and MAM was from the southeast rather than the nominal northeast. Therefore, careful attention should be given to this shift, and on-site investigations should be conducted for confirmation prior to any offshore project implementation.

The wind resource maps show that the annual average wind speed over the EEZ was 5.15 m/s, 5.20 m/s, and 5.27 m/s and that the WPD was 188.75 W/m², 197.68 W/m², and 207.89 W/m² at 80 m, 100 m, and 140 m ASL, respectively. The predominant wind direction came from the

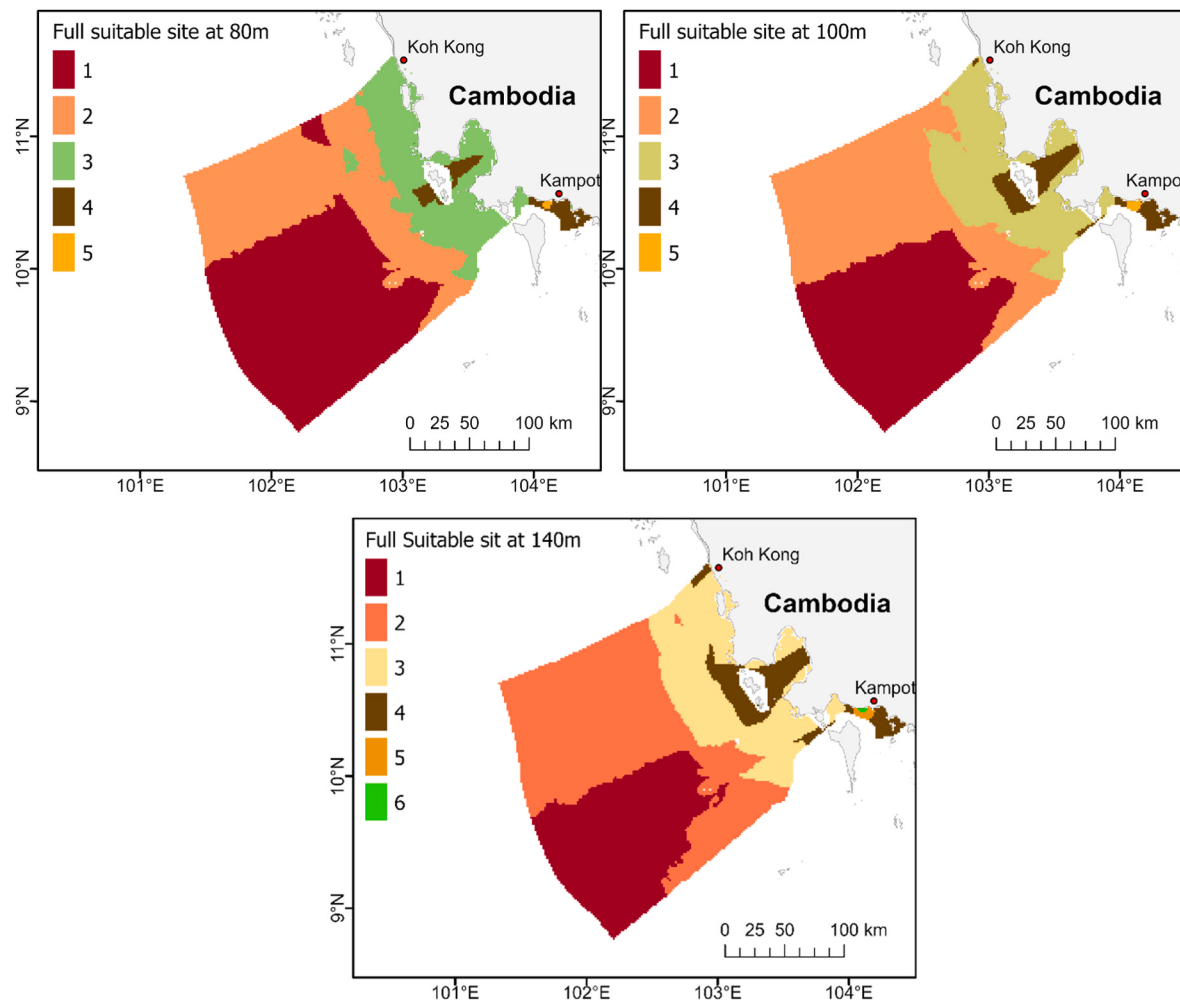


Fig. 13. The indexes marking the levels of suitability for an offshore wind farm within the EEZ at 80 m, 100 m and 140 m ASL for the second scenario. Two marine protective zones, Koh Rung Marine National Park and Ream National Park, are excluded. Levels 4–6 are suitable for offshore wind farms.

Table 8

Annual energy production (AEP) by turbine foundation types and equivalent CO₂ amount for the first 15 km-offset scenario.

Height ASL	Types of foundations	Area (km ²)	Numbers of turbines	Mean CF	AEP (GWh)	CO ₂ equivalent (Mt-CO ₂ /y)
80 m	Monopile	109.98	175	0.23	927.00	0.42
100 m	Monopile	241.96	180	0.19	2049.20	0.94
40 m	Monopile	472.93	195	0.23	4031.01	1.85
	Lattice Monopile	30.24	12	0.22	237.27	0.11
<i>Total</i>		<i>503.17</i>	<i>207</i>		<i>4268.28</i>	<i>1.96</i>

Table 9

AEP by turbine foundation types and equivalent CO₂ amount for the second scenario.

Height ASL	Types of foundations	Area (km ²)	Numbers of turbines	Mean CF	AEP (GWh)	CO ₂ equivalent (Mt-CO ₂ /y)
80 m	Monopile	1163.08	1854	0.27	11528.93	5.29
	Lattice monopile	35.74	57	0.32	420.09	0.19
<i>Total</i>		<i>1198.82</i>	<i>1911</i>		<i>11949.02</i>	<i>5.48</i>
100 m	Monopile	1990.71	1480	0.22	19509.43	8.95
	Lattice monopile	38.49	29	0.29	503.91	0.23
<i>Total</i>		<i>2029.20</i>	<i>1509</i>		<i>20013.34</i>	<i>9.18</i>
140 m	Monopile	3346.27	1383	0.25	31075.18	14.26
	Lattice monopile	76.99	32	0.28	805.30	0.37
<i>Total</i>		<i>3423.26</i>	<i>1415</i>		<i>31880.48</i>	<i>14.63</i>

Table 10

Comparison of spatially averaged wind speeds over the Cambodian EEZ at 140 m and 150 m heights for the windiest season (June, July, and August (JJA)) in 2019.

Wind speed	Height (ASL)		Difference (m/s)	Increment (%)
	140 m	150 m		
Mean (m/s)	6.766	6.793	0.027	0.40
Max (m/s)	9.425	9.469	0.044	0.47
Min (m/s)	3.621	3.634	0.013	0.36

south. The highest annual mean wind speed of 6–7.22 m/s, 7.45 m/s, or 7.62 m/s ($WPD > 300 \text{ W/m}^2$) occurred along the shorelines of the Kampot and Kep Provinces, indicating that the EEZ is potentially promising for future offshore projects, especially along the Kampot and Kep Provinces.

By erecting the V112, V164, and HX12 turbines in optimal areas of 109.98 km^2 , 241.96 km^2 , and 503.17 km^2 in the first 15 km-offset scenario, respectively, the resulting AEP was estimated to be 927.00 GWh, 2049.20 GWh, and 4265.28 GWh which could help reduce the amount of CO₂ emissions by 0.42 Mt-CO₂, 0.94 Mt-CO₂, and 1.96 Mt-CO₂ per year, respectively. If 10% of the total AEP could be generated by 2030, the offshore wind source would contribute to 0.15%, 0.33%, or 0.69% of the country's electric demands forecasted for 2030.

In the second scenario, the remarkable increase of optimal areas of 1198.82 km^2 , 2029.20 km^2 , and 3423.26 km^2 at 80 m, 100 m, and 140 m ASL led to more numbers of V112 (1911), V164 (1509), and HX12 (1415) turbines, yielding the total AEP of 11,949.02 GWh, 20,013.34 GWh, and 31,880.48 GWh, respectively. They were estimated to annually reduce the amount of CO₂ emissions by 5.48 Mt-CO₂ with V112, 9.18 Mt-CO₂ with V164, and 14.63 Mt-CO₂ with HX12. If 10% of the total AEP could be generated by 2030, the offshore wind source would contribute to 1.95%, 3.27%, or 5.20% of the country's electric demands forecasted for 2030.

This study has constraints regarding onshore in situ wind data. For a better representation of the offshore wind characteristics, off-coast or near-coast measurements should be used instead of the current inland AWSs. Equally importantly, the observed vertical wind should be available for validation and construction of the local wind profile. These in situ wind observations would help promote understanding of the model's capability as well as inconsistency in the prediction of offshore winds in the Cambodian EEZ both horizontally and vertically.

Appendix A. Information about the wind turbines

Table A1

Summary of technical specifications of the three selected offshore wind turbines

Model	V112	V164	HX12
Manufacturer	Vestas	Vestas	General Electric
Rated power (MW)	3.0	8.0	12.0
Cut-in wind speed (m/s)	3.0	4.0	3.0
Rated wind speed (m/s)	12.0	13.0	13.0
Cut-out wind speed (m/s)	25.0	25.0	25.0
Diameter (m)	112.0	164.0	220.0
Swept area (m ²)	9852.0	21,124.0	38,000.0
Hub height (m)	84/119 [78]	105/140 [13,16]	150 [59,60]

Despite certain limitations, the findings in the present study could enable use of the WRF model as an acceptable method for assessing offshore wind resources and offshore wind power in places where offshore in situ data do not exist. The findings also introduce another new understanding of the comparison between the WRF resulting winds and the Sentinel-1 L2 OCN product, which has not yet been widely employed in wind resource evaluations. This study would also become a reference for future research interested in such a comparison, and in a broader sense, this study would be a primary contribution in planning future renewable energy development in Cambodia in terms of offshore wind.

Funding

This research did not receive any specific grant from funding agencies in the public, commercial, or not-for-profit sectors.

Data availability

All data and resources are available from the authors upon requests.

CRediT author statement

Soklin Tuy, Han Soo Lee, Karodine Chreng: Conceptualization, Methodology, Software, Data curation, Writing- Original draft preparation, Visualization, Investigation, Software, Validation.: **Han Soo Lee:** Supervision, Writing- Reviewing and Editing.

Declaration of competing interest

The authors declare that they have no known competing financial interests or personal relationships that could have appeared to influence the work reported in this paper.

Acknowledgements

The first and third authors are supported by the Project for Human Resource Development Scholarship (JDS), Japan. The authors would like to express gratitude to the Department of Meteorology of MOW-RAM, which provided the in-situ data at the four AWSs. The weather data are available upon request.

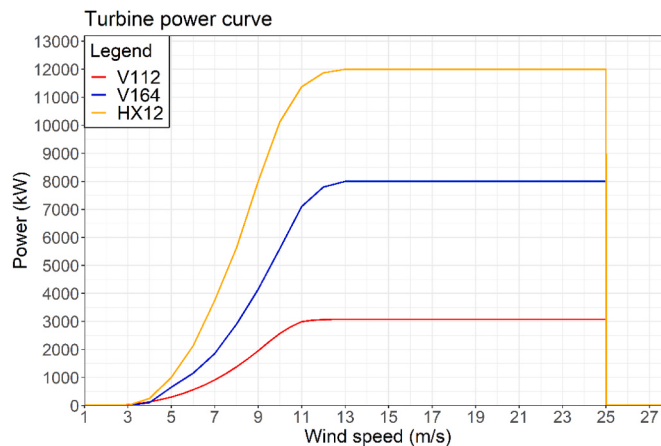


Fig. A1. Power curves of turbine models V112 (red), V164 (blue), and HX12 (orange).

Appendix B. Supplementary data

Supplementary data to this article can be found online at <https://doi.org/10.1016/j.rser.2022.112501>.

References

- [1] Ren21. Renewables 2020 global status report. Paris, France: REN21 Secretariat; 2020.
- [2] Lee J, Zhao F, Dutton A, Backwell B, Fiestas R, Qiao L, Balachandran N, Lim S, Liang W, Clarke E, Lathigara A, Younger DR. GWEC_Global wind report 2021. 2021. Brussels, Belgium, <https://gwec.net/global-wind-report-2021/>. [Accessed 5 November 2021].
- [3] International Energy Agency. Offshore wind outlook 2019: world energy outlook special report. 2019.
- [4] Chang R, Zhu R, Badger M, Hasager CB, Xing X, Jiang Y. Offshore wind resources assessment from multiple satellite data and WRF modeling over South China Sea. *Rem Sens* 2015;7:467–87. <https://doi.org/10.3390/rs70100467>.
- [5] Hong L, Möller B. Offshore wind energy potential in China: under technical, spatial and economic constraints. *Energy* 2011;36:4482–91. <https://doi.org/10.1016/j.energy.2011.03.071>.
- [6] Arun Kumar SVV, Nagababu G, Kumar R. Comparative study of offshore winds and wind energy production derived from multiple scatterometers and met buoys. *Energy* 2019;185:599–611. <https://doi.org/10.1016/j.energy.2019.07.064>.
- [7] Nagababu G, Kachhwaha SS, Savsani V. Estimation of technical and economic potential of offshore wind along the coast of India. *Energy* 2017;138:79–91. <https://doi.org/10.1016/j.energy.2017.07.032>.
- [8] Gadad S, Deka PC. Offshore wind power resource assessment using Oceansat-2 scatterometer data at a regional scale. *Appl Energy* 2016;176:157–70. <https://doi.org/10.1016/j.apenergy.2016.05.046>.
- [9] Sheridan B, Baker SD, Pearre NS, Firestone J, Kempton W. Calculating the offshore wind power resource: robust assessment methods applied to the U.S. Atlantic Coast. *Renew Energy* 2012;43:224–33. <https://doi.org/10.1016/j.renene.2011.11.029>.
- [10] Tuchtenhagen P, de Carvalho GG, Martins G, da Silva PE, de Oliveira CP, de Melo Barbosa Andrade L, de Araújo JM, Mutti PR, Lucio PS, Silva CMSe. WRF model assessment for wind intensity and power density simulation in the southern coast of Brazil. *Energy* 2020;190. <https://doi.org/10.1016/j.energy.2019.116341>.
- [11] Vinhoza A, Schaeffer R. Brazil's offshore wind energy potential assessment based on a Spatial Multi-Criteria Decision Analysis. *Renew Sustain Energy Rev* 2021;146. <https://doi.org/10.1016/j.rser.2021.111185>.
- [12] González-Alonso de Linaje N, Mattar C, Borvarán D. Quantifying the wind energy potential differences using different WRF initial conditions on Mediterranean coast of Chile. *Energy* 2019;188. <https://doi.org/10.1016/j.energy.2019.116027>.
- [13] Mattar C, Borvarán D. Offshore wind power simulation by using WRF in the central coast of Chile. *Renew Energy* 2016;94:22–31. <https://doi.org/10.1016/j.renene.2016.03.005>.
- [14] Hasager CB, Hahmann AN, Ahsbahs T, Karagali I, Sile T, Badger M, Mann J. Europe's offshore winds assessed with synthetic aperture radar, ASCAT and WRF. *Wind Energy Sci* 2020;5:375–90. <https://doi.org/10.5194/wes-5-375-2020>.
- [15] Hasager CB, Mouche A, Badger M, Bingöl F, Karagali I, Driesenaar T, Stoffelen A, Peña A, Longépé N. Offshore wind climatology based on synergistic use of Envisat ASAR, ASCAT and QuikSCAT. *Rem Sens Environ* 2015;156:247–63. <https://doi.org/10.1016/j.rse.2014.09.030>.
- [16] Quang VD, Doan VQ, Dinh VN, Dinh N, Uyen VNL, Anh NP, Van NTT, Tri N, v Minh N, Huy NN, v Linh T, Gaspillo P, Ha HKP, Hoang TV, Le HT, Thanh N, Truong T, Nguyen HT, Nguyen LT, Song D, Truong TT, Nguyen T, Tuyet T, Phan M, sen Ngo T, Nguyen TH, Thanh L, Huynh N, Linh TP, Le VH, Xuan PM, Tran LH, Ky H, Ha P, Phong MT, Huang C. Evaluation of resource spatial-temporal variation, dataset validation, infrastructures and zones for Vietnam offshore wind energy.pdf. *Vietnam J Sci Technol Eng* 2019;62:1–16. [https://doi.org/10.31276/VJSTE.62\(1\).03-16](https://doi.org/10.31276/VJSTE.62(1).03-16).
- [17] Doan VQ, Dinh VN, Kusaka H, Cong T, Khan A, Van Toan D, Duc ND. Usability and challenges of offshore wind energy in Vietnam revealed by the regional climate model simulation. *Sci Online Lett Atmos* 2019;15:113–8. <https://doi.org/10.2151/SOLA.2019-021>.
- [18] Chancham C, Waewsak J, Gagnon Y. Offshore wind resource assessment and wind power plant optimization in the Gulf of Thailand. *Energy* 2017;139:706–31. <https://doi.org/10.1016/j.energy.2017.08.026>.
- [19] Waewsak J, Landry M, Gagnon Y. Offshore wind power potential of the Gulf of Thailand. *Renew Energy* 2015;81:609–26. <https://doi.org/10.1016/j.renene.2015.03.069>.
- [20] Ranftod sang M, Waewsak J, Kongruang C, Gagnon Y. Offshore wind power assessment on the western coast of Thailand. *Energy Rep* 2020;6:1135–46. <https://doi.org/10.1016/j.jegyr.2020.04.036>.
- [21] Tuy S, Lee HS, Chreng K. Offshore wind resource mapping in Cambodia: sensitivity assessment of the weather research and forecasting model. *Energy Rep* 2022;8: 359–64. <https://doi.org/10.1016/j.jegyr.2022.01.065>.
- [22] Carvalho D, Rocha A, Gómez-Gesteira M, Silva Santos C. Comparison of reanalyzed, analyzed, satellite-retrieved and NWP modelled winds with buoy data along the Iberian Peninsula coast. *Rem Sens Environ* 2014;152:480–92. <https://doi.org/10.1016/j.rse.2014.07.017>.
- [23] Salvação N, Guedes Soares C. Wind resource assessment offshore the Atlantic Iberian coast with the WRF model. *Energy* 2018;145:276–87. <https://doi.org/10.1016/j.energy.2017.12.101>.
- [24] Carvalho D, Rocha A, Gómez-Gesteira M, Santos C. A sensitivity study of the WRF model in wind simulation for an area of high wind energy. *Environ Model Software* 2012;33:23–34. <https://doi.org/10.1016/j.envsoft.2012.01.019>.
- [25] Mai X, Ma Y, Yang Y, Li D, Qiu X. Impact of grid nudging parameters on dynamical downscaling during summer over mainland China. *Atmosphere* 2017;8. <https://doi.org/10.3390/atmos8100184>.
- [26] Dzebre DEK, Acheampong AA, Ampofo J, Adaramola MS. A sensitivity study of surface wind simulations over coastal Ghana to selected time control and nudging options in the weather research and forecasting model. *Heliyon* 2019;5:e01385. <https://doi.org/10.1016/j.heliyon.2019.e01385>.
- [27] Ma Y, Yang Y, Mai X, Qiu C, Long X, Wang C. Comparison of analysis and spectral nudging techniques for dynamical downscaling with the WRF model over China. *Adv Meteorol* 2016;2016:4761513. <https://doi.org/10.1155/2016/4761513>.
- [28] Chadee XT, Seegobin NR, Clarke RM. Optimizing the weather research and forecasting (WRF) model for mapping the near-surfacewind resources over the southernmost caribbean islands of Trinidad and Tobago. *Energies* 2017;10. <https://doi.org/10.3390/en10070931>.
- [29] Gómez-Navarro JJ, Raible CC, Dierer S. Sensitivity of the WRF model to PBL parametrizations and nesting techniques: evaluation of wind storms over complex terrain. *Geosci Model Dev (GMD)* 2015;8:3349–63. <https://doi.org/10.5194/gmd-8-3349-2015>.
- [30] Witha B, Hahmann AN, Sile T, Dörenkämper M, Ezber Y, García-Bustamante E, González-Rouco JF, Leroy G, Navarro J. Report on WRF model sensitivity studies and specifications for the mesoscale wind atlas production runs: deliverable V4, vol. 3; 2019. <https://doi.org/10.5281/zenodo.2682604>.

- [31] Lee HS, Yamashita T, Hsu John R-C, Ding F. Integrated modeling of the dynamic meteorological and sea surface conditions during the passage of Typhoon Morakot. *Dynam Atmos Oceans* 2013;59:1–23. <https://doi.org/10.1016/j.dynatmoce.2012.09.002>.
- [32] Lo JC-F, Yang Z-L, Pielke RA. Assessment of three dynamical climate downscaling methods using the Weather Research and Forecasting (WRF) model. *J Geophys Res* 2008;113. <https://doi.org/10.1029/2007jd009216>.
- [33] Bowden JH, Otte TL, Nolte CG, Otte MJ. Examining interior grid nudging techniques using two-way nesting in the WRF model for regional climate modeling. *J Clim* 2012;25:2805–23. <https://doi.org/10.1175/JCLI-D-11-00167.1>.
- [34] Vincent CL, Hahmann AN. The impact of grid and spectral nudging on the variance of the near-surface wind speed. *J Appl Meteorol Climatol* 2015;54:1021–38. <https://doi.org/10.1175/JAMC-D-14-0047.1>.
- [35] Hasager CB. Offshore winds mapped from satellite remote sensing. *Wiley Interdiscipl Rev: Energy Environ* 2014;3:594–603. <https://doi.org/10.1002/wene.123>.
- [36] Ahsbahs T, Badger M, Karagali I, Larsén XG. Validation of sentinel-1A SAR coastal wind speeds against scanning LiDAR. *Rem Sens* 2017;9:1–17. <https://doi.org/10.3390/rs9060552>.
- [37] Majidi Nezhad M, Groppi D, Marzialetti P, Fusilli L, Laneve G, Cumo F, Garcia DA. Wind energy potential analysis using Sentinel-1 satellite: a review and a case study on Mediterranean islands. *Renew Sustain Energy Rev* 2019;109:499–513. <https://doi.org/10.1016/j.rser.2019.04.059>.
- [38] De Montera L, Remmers T, O'Connell R, Desmond C. Validation of Sentinel-1 offshore winds and average wind power estimation around Ireland. *Wind Energy Sci* 2020;5:1023–36. <https://doi.org/10.5194/wes-5-1023-2020>.
- [39] Hadjipetrou S, Lioudakis S, Sykioti A, Fayad P, Akylas E, Park N-W, et al. Preliminary assessment of offshore wind speed around Cyprus based on Sentinel-1 Level 2 OCN data. *Proc SPIE* 2020;11524. <https://doi.org/10.1117/12.2571945>.
- [40] Bentamy A, Mouche A, Grouazel A, Moujane A, Mohamed AA. Using sentinel-1A SAR wind retrievals for enhancing scatterometer and radiometer regional wind analyses. *Int J Rem Sens* 2018;40:1120–47. <https://doi.org/10.1080/01431161.2018.1524174>.
- [41] Asian Development Bank. *Country partnership strategy: Cambodia, 2019–2023 –inclusive pathways to a competitive economy*. 2019.
- [42] Electricity Authority of Cambodia. Salient feature of power development in the Kingdom of Cambodia until December 2020: consolidated report for the year 2020. 2020. <https://www.eac.gov.kh/site/index?lang=en>.
- [43] Janjai S, Pankaew P, Laksanaboonsong J, Kitichantaropas P. Estimation of solar radiation over Cambodia from long-term satellite data. *Renew Energy* 2011;36:1214–20. <https://doi.org/10.1016/j.renene.2010.09.023>.
- [44] Pagnarik K, Limmeechokchai B. Biomass and solar energy for rural electrification and CO₂ mitigation in Cambodia. *Int J Relig Educ* 2009;4:25–34. [http://www.sert.nu.ac.th/IIRE/V4N2\(3\).pdf](http://www.sert.nu.ac.th/IIRE/V4N2(3).pdf).
- [45] Sarraf M, Rismanchi B, Saidur R, Ping HW, Rahim NA. Renewable energy policies for sustainable development in Cambodia. *Renew Sustain Energy Rev* 2013;22:223–9. <https://doi.org/10.1016/j.rser.2013.02.010>.
- [46] TrueWind Solutions L. *Wind energy resource atlas of Southeast Asia (English)*. Washington, DC: World Bank Group; 2001.
- [47] Janjai S, Promsen W, Masiri I, Laksanaboonsong J. *Wind resource maps for Cambodia*. *J Sustain Energy Environ* 2013;4:159–64.
- [48] Promsen W, Janjai S, Tantalechon T. An analysis of wind energy potential of Kampot province, southern Cambodia. In: Organizing committee of 2013 AEDCEE. *Energy Procedia*, Elsevier Ltd; 2014. p. 633–41. <https://doi.org/10.1016/j.egypro.2014.07.119>.
- [49] Raza Rizvi A, Singer U. *Cambodia coastal situational analysis*. Gland, Switzerland: IUCN; 2011.
- [50] The European Space Agency. Sentinel-1 overview. 2021. <https://sentinel.esa.int/web/sentinel/missions/sentinel-1/overview>. [Accessed 5 May 2021].
- [51] Copernicus Open Access Hub, (n.d.).
- [52] Mouche A, Vincent P. Sentinel-1 ocean wind fields (OWI) algorithm definition. 2011. <https://sentinel.esa.int/documents/247904/3861173/Sentinel-1-Ocean-Wind-Fields-OWI-ATBD.pdf>.
- [53] Vincent P, Bourbigot M, Johnsen H, Piantanida R. Sentinel-1 product specification. 2020. <https://sentinel.esa.int/documents/247904/1877131/Sentinel-1-Product-Specification>.
- [54] Skamarock WC, Klemp JB, Dudhia JB, Gill DO, Barker DM, Duda MG, Huang X-Y, Wang W, Powers JG. A description of the advanced research WRF version 3, mesoscale and microscale Meteorology division. Boulder, Colorado, USA: National Center for Atmospheric Research; 2008.
- [55] Hersbach H, Bell B, Berrisford P, Hirahara S, Horányi A, Muñoz-Sabater J, Nicolas J, Peubey C, Radu R, Schepers D, Simmons A, Soci C, Abdalla S, Abellán X, Balsamo G, Bechtold P, Biavati G, Bidlot J, Bonavita M, De Chiara G, Dahlgren P, Dee D, Diamantakis M, Dragani R, Flemming J, Forbes R, Fuentes M, Geer A, Haimberger L, Healy S, Hogan RJ, Hólm E, Janisková M, Keeley S, Laloyaux P, Lopez P, Lupu C, Radnoti G, de Rosnay P, Rozum I, Vamborg F, Villame S, Thépaut JN. The ERA5 global reanalysis. *Q J R Meteorol Soc* 2020;146:1999–2049. <https://doi.org/10.1002/qj.3803>.
- [56] Wang W, Bruyere C, Duda M, Dudhia J, Gill D, Kavulich M, Keene K, Chen M, Lin H-C, Michalakes J, Rizvi S, Zhang X, Berner J, Ha S, Fossell K. In: WRF-ARW V3: user's guide. WRF USERS PAGE; 2017. p. 443. https://www2.mmm.ucar.edu/wrf/users/docs/user_guide_V3/user_guide_V3.9/contents.html. [Accessed 16 May 2021].
- [57] Jiménez-Guerrero P, Jordà O, Baldasano JM, Gassó S. The use of a modelling system as a tool for air quality management: annual high-resolution simulations and evaluation. *Sci Total Environ* 2008;390:323–40. <https://doi.org/10.1016/j.scitotenv.2007.10.025>.
- [58] Carvalho D, Rocha A, Gómez-Gesteira M, Silva Santos C. Offshore winds and wind energy production estimates derived from ASCAT, OSCAT, numerical weather prediction models and buoys – a comparative study for the Iberian Peninsula Atlantic coast. *Renew Energy* 2017;102:433–44. <https://doi.org/10.1016/j.renene.2016.10.063>.
- [59] wind-turbine-models.com. n.d. <https://en.wind-turbine-models.com/>.
- [60] Saint-Drenan YM, Besseau R, Jansen M, Staffell I, Troccoli A, Dubus L, Schmidt J, Gruber K, Simões SG, Heier S. A parametric model for wind turbine power curves incorporating environmental conditions. *Renew Energy* 2020;157:754–68. <https://doi.org/10.1016/j.renene.2020.04.123>.
- [61] Manwell JF, McGowan JG, Rogers AL. *Wind energy explained: theory, design and application*. second ed. United Kingdom: John Wiley & Sons Ltd.; 2009.
- [62] Elliott DL, Holladay CG, Barchet WR, Foote HP, Sandusky WF. Wind energy resource atlas of the United States, United States. 1987. <https://www.osti.gov/biblio/6628633>.
- [63] Elliott D, Schwartz M. Development and validation of high-resolution state wind resource maps for the United States. 2005. <http://www.osti.gov/bridge>.
- [64] Sullivan RG, Kirchler LB, Cothren J, Winters SL. Offshore wind turbine visibility and visual impact threshold distances offshore wind turbine visibility 1. 2013. <https://doi.org/10.1017/S1466046612000464>.
- [65] Barthelmie RJ, Frandsen ST, Nielsen MN, Pryor SC, Rethore PE, Jørgensen HE. Modelling and measurements of power losses and turbulence intensity in wind turbine wakes at middelgrunden offshore wind farm. *Wind Energy* 2007;10:517–28. <https://doi.org/10.1002/we.238>.
- [66] The United Nations. Methodological tool: tool to calculate the emission factor for an electricity system version 05.0. 2015. <https://cdm.unfccc.int/methodologies/PAmethodologies/tools/am-tool-07-v5.0.pdf>. [Accessed 7 June 2021].
- [67] Institute for Global Environmental Strategies. Grid emission factors in Cambodia. 2016. https://portal.gms-eoc.org/uploads/resources/1904/attachment/GEF-Cambodia_2010-2012.pdf. [Accessed 7 June 2021].
- [68] Saaty TL. *The analytic hierarchy process: planning, priority setting, resource allocation*. McGraw-Hill; 1980.
- [69] Odu GO. Weighting methods for multi-criteria decision making technique. *J Appl Sci Environ Manag* 2019;23:1449–57. <https://doi.org/10.4314/jasem.v23i8.7>.
- [70] Cabrera JS, Lee HS. Impacts of climate change on flood-prone area in Davao Oriental, Philippines. *Water* 2018;10(7):893. <https://doi.org/10.3390/w10070893>.
- [71] Cabrera JS, Lee HS. Flood-prone area assessment using GIS-based multi-criteria analysis: a case study in Davao Oriental. 2019. p. 11. <https://doi.org/10.3390/w1112203>. Philippines, Water (Switzerland).
- [72] Cabrera JS, Lee HS. Flood risk assessment for Davao Oriental in the Philippines using geographic information system-based multi-criteria analysis and the maximum entropy model. *J Flood Risk Manag* 2020;13. <https://doi.org/10.1111/jfr3.12607>.
- [73] Carvalho D, Rocha A, Gómez-Gesteira M, Silva Santos C. WRF wind simulation and wind energy production estimates forced by different reanalyses: comparison with observed data for Portugal. *Appl Energy* 2014;117:116–26. <https://doi.org/10.1016/j.apenergy.2013.12.001>.
- [74] Santos-Alamillos FJ, Pozo-Vazquez D, Ruiz-arias JA, Fanego-Lara V, Tovar-Pescador J. Analysis of WRF model wind estimate sensitivity to physics parameterization choice and terrain representation in Andalusia (Southern Spain). *J Appl Meteorol Climatol* 2013;52:1592–609. <https://doi.org/10.1175/JAMC-D-12-0204.1>.
- [75] Hariprasad KBRR, v Srinivas C, Singh AB, Bhaskara SV, Baskaran R, Venkatraman B. Numerical simulation and intercomparison of boundary layer structure with different PBL schemes in WRF using experimental observations at a tropical site. *Atmos Res* 2014;145–146:27–44. <https://doi.org/10.1016/j.atmos.2014.03.023>.
- [76] Barthelmie RJ, Pryor SC. Can satellite sampling of offshore wind speeds realistically represent wind speed distributions? *J Appl Meteorol* 2003;42:83–94. [https://doi.org/10.1175/1520-0450\(2003\)042<0083](https://doi.org/10.1175/1520-0450(2003)042<0083).
- [77] Nagababu G, Naidu NK, Kachhwaha SS, Savsani V. Feasibility study for offshore wind power development in India based on bathymetry and reanalysis data. *Energy Sources, Part A Recovery, Util Environ Eff* 2017;39:497–504. <https://doi.org/10.1080/15567036.2016.1233303>.
- [78] The Wind Power. The wind power: wind energy market intelligence. 2021. https://www.thewindpower.net/turbine_en_413 Vestas_v112-3000.php. [Accessed 18 July 2021].
- [79] Lee HS. Evaluation of WAVEWATCH III performance with wind input and dissipation source terms using wave buoy measurements for October 2006 along the east Korean coast in the East Sea. *Ocean Eng* 2015;100:67–82. <https://doi.org/10.1016/j.oceaneng.2015.03.009>.